nature medicine

Article

https://doi.org/10.1038/s41591-024-03010-w

Noninvasive assessment of organ-specific and shared pathways in multi-organ fibrosis using T1 mapping

Received: 5 September 2023

Accepted: 22 April 2024

Published online: 28 May 2024

Check for updates

A list of authors and their affiliations appears at the end of the paper

Fibrotic diseases affect multiple organs and are associated with morbidity and mortality. To examine organ-specific and shared biologic mechanisms that underlie fibrosis in different organs, we developed machine learning models to quantify T1 time, a marker of interstitial fibrosis, in the liver, pancreas, heart and kidney among 43,881 UK Biobank participants who underwent magnetic resonance imaging. In phenome-wide association analyses, we demonstrate the association of increased organ-specific T1 time, reflecting increased interstitial fibrosis, with prevalent diseases across multiple organ systems. In genome-wide association analyses, we identified 27, 18, 11 and 10 independent genetic loci associated with liver, pancreas, myocardial and renal cortex T1 time, respectively. There was a modest genetic correlation between the examined organs. Several loci overlapped across the examined organs implicating genes involved in a myriad of biologic pathways including metal ion transport (*SLC39A8, HFE* and *TMPRSS6*), glucose metabolism (*PCK2*), blood group antigens (*ABO* and *FUT2*), immune function (*BANK1* and *PPP3CA*), inflammation (*NFKB1*) and mitosis (*CENPE*). Finally, we found that an increasing number of organs with T1 time falling in the top quintile was associated with increased mortality in the population. Individuals with a high burden of fibrosis in ≥3 organs had a 3-fold increase in mortality compared to those with a low burden of fibrosis across all examined organs in multivariable-adjusted analysis (hazard ratio = 3.31, 95% confidence interval 1.77–6.19; $P = 1.78 \times 10^{-4}$). By leveraging machine learning to quantify T1 time across multiple organs at scale, we uncovered new organ-specific and shared biologic pathways underlying fibrosis that may provide therapeutic targets.

Approximately 45% of deaths in the United States are attributed to fibrotic diseases most commonly affecting the heart, liver, kidneys and lungs[1]. With an aging population, the burden of fibrotic diseases will continue to rise in the face of limited effective therapies[2]. Understanding the prevalence of multi-organ interstitial fibrosis in the general population and unraveling shared and organ-specific mechanisms underlying fibrosis is essential to devise interventions and therapies to curb the rising burden of fibrotic diseases.

Magnetic resonance T1 mapping enables noninvasive assessment of interstitial fibrosis across multiple organs[3–6]. The UK Biobank (UKB) is a large biorepository containing in-depth genetic and health information for over half a million prospective participants. Of these participants, approximately 44,000 participants underwent additional imaging using dedicated multi-organ magnetic resonance imaging (MRI) with T1 mapping. In this study, we leverage the UKB to (1) develop machine learning models to quantify T1 time of the liver, pancreas,

e-mail: ellinor@mgh.harvard.edu

heart and kidney at scale, (2) examine the implications of organ-specific T1 time on disease in the population, and (3) explore the organ-specific and shared genetic determinants of fibrosis using genetic association studies.

Results

Machine learning enables quantification of T1 time at scale

We examined 43,881 participants with both MRI T1 mapping and imputed genotype data in the UKB. Dedicated organ-specific T1 mapping using the Shortened Modified Look-Locker Inversion recovery (ShMOLLI, WIP780B) technique was performed on the liver, pancreas, heart and kidneys in the UKB (Methods). The mean age of the study participants was 64.2 ± 7.7 years, and 48.5% were males (Table 1). T1 mapping data for the liver, pancreas, heart and renal cortex were available for 36,516, 33,862, 39,339 and 30,155 participants, respectively (Supplementary Fig. 1). To measure the T1 times for specific organs, we constructed machine learning models to segment the liver, heart, pancreas and renal cortex from T1 maps (Fig. 1 and Methods). Notably, since only 1,893 participants had coronal kidney-specific T1 mapping, we leveraged the inclusion of kidney axial cross-sections within the pancreas T1 maps to expand our sample size by ~16-fold. Only the renal cortex was adequately sampled in the axial images and as such we focused on renal cortex T1 time in this study. We verified that the T1 times from both the coronal and axial acquisitions of the kidney had good concordance among participants who underwent both imaging acquisitions (renal cortex (n = 621): r = 0.68, 95% confidence interval (CI) 0.65–0.72, $P = 2.61 \times 10^{-111}$) supporting the use of kidney axial acquisitions for measurement of T1 time (Supplementary Fig. 2). Both axial and coronal/oblique-coronal axes have been recommended for quantification of renal T1 time[7].

In a hold-out validation set, we confirmed that manually derived organ-specific T1 times by experienced physicians and machine learning model-derived T1 times were highly concordant for all four examined organs (Methods and Supplementary Figs. 3–6).

Organ-specific T1 times were overall normally distributed in our study sample (Supplementary Fig. 7). Median T1 time and interquartile range (IQR) for each organ are reported in Table 1. Median T1 time of the pancreas, heart and renal cortex was greater in females than males (standardized mean difference: pancreas 25.76%, heart 24.93% and renal cortex 10.04%), while median liver T1 time was higher in males compared to females (standardized mean difference 12.53%). Across increasing decades of age in the study sample, pancreas and renal cortex T1 time increased in both males and females, while heart T1 time decreased with age in females and increased with age in males. There was no significant trend for change in liver T1 time with increasing decades of age across both strata of sex (Supplementary Fig. 8).

Inter-organ T1 time correlation was overall weak. The strongest correlations, albeit modest, were between the renal cortex T1 time and both liver T1 time (r = 0.25, 95% CI 0.24–0.26; P value = 3.24×10^{-219}) and pancreas T1 time (r = 0.17, 95% CI 0.16–0.18; P value = 2.67×10^{-178}; Supplementary Fig. 9).

Fibrosis is associated with disease in multiple organ systems

In a phenome-wide association analysis (PheWAS), we identified a consistent association of increased organ-specific T1 time with prevalent diseases across multiple organ systems (Fig. 2a and Supplementary Fig. 10). Higher organ-specific T1 time was particularly associated with diseases affecting the respective organ system. However, we also noted associations between organ-specific T1 times and diseases affecting other organ systems, highlighting multi-organ involvement in certain chronic diseases. Two-sided P values < 4×10^{-5} were considered statistically significant.

Liver T1 time had the highest number of disease associations compared to the other examined organs. Among gastrointestinal diseases, higher liver T1 time was associated with increased odds of liver cirrhosis (odds ratio (OR) per standard deviation (s.d.) ($OR_{/s.d.}$ = 1.58, 95% CI 1.41–1.78; $P = 2.94 \times 10^{-14}$), abnormal liver function studies ($OR_{/s.d.}$ = 1.33, 95% CI 1.20–1.47; $P = 1.02 \times 10^{-7}$), inflammatory bowel disease ($OR_{/s.d.}$ = 1.28, 95% CI 1.14–1.43; $P = 2.66 \times 10^{-5}$) and cholelithiasis/cholecystitis ($OR_{/s.d.}$ = 1.24, 95% CI 1.17–1.31; $P = 1.72 \times 10^{-12}$). In addition, several notable associations between increased liver T1 time and cardiovascular, respiratory, endocrine, metabolic and systemic inflammatory disorders were identified (Fig. 2a and Supplementary Table 1).

In the pancreas, higher T1 time was associated with increased odds of diseases of the pancreas ($OR_{/s.d.}$ = 1.48, 95% CI 1.25–1.76; $P = 5.56 \times 10^{-6}$), functional digestive disorders ($OR_{/s.d.}$ = 1.11, 95% CI 1.06–1.15; $P = 1.51 \times 10^{-6}$), abdominal pain ($OR_{/s.d.}$ = 1.08, 95% CI 1.04–1.12; $P = 2.00 \times 10^{-5}$) and esophageal disorders ($OR_{/s.d.}$ = 1.11, 95% CI 1.08–1.15; $P = 1.39 \times 10^{-9}$). Notably, there was a strong association between pancreas T1 time and prevalent type 1 diabetes mellitus ($OR_{/s.d.}$ = 1.68, 95% CI 1.39–2.03; $P = 8.58 \times 10^{-8}$; Fig. 2a and Supplementary Table 2).

In the heart, myocardial T1 time was associated with several cardiopulmonary disorders including heart failure ($OR_{/s.d.}$ = 1.40, 95% CI 1.19–1.64; $P = 3.86 \times 10^{-5}$), conduction disease ($OR_{/s.d.}$ = 1.30, 95% CI 1.16–1.45; $P = 3.37 \times 10^{-6}$), chronic obstructive airway disease ($OR_{/s.d.}$ = 1.46, 95% CI 1.33–1.61; $P = 8.96 \times 10^{-16}$) and asthma ($OR_{/s.d.}$ = 1.19, 95% CI 1.14–1.24; $P = 3.52 \times 10^{-17}$). Additionally, myocardial T1 time was associated with increased odds of type 2 diabetes mellitus ($OR_{/s.d.}$ = 1.26, 95% CI 1.19–1.34; $P = 2.90 \times 10^{-15}$; Fig. 2a and Supplementary Table 3).

In the kidney, higher renal cortex T1 time was associated with increased odds of both acute ($OR_{/s.d.}$ = 1.53, 95% CI 1.29–1.82; $P = 1.02 \times 10^{-6}$) and chronic ($OR_{/s.d.}$ = 1.49, 95% CI 1.30–1.70; $P = 3.63 \times 10^{-9}$) renal failure. Additionally, renal cortex T1 time was associated with the presence of kidney cysts ($OR_{/s.d.}$ = 1.53, 95% CI 1.28–1.83; $P = 3.17 \times 10^{-6}$), hypertension ($OR_{/s.d.}$ = 1.14, 95% CI 1.10–1.18;

Table 1 | Study sample characteristics at time of first visit for MRI

Baseline characteristics	N = 43,881 (%)
Age at MRI, years (mean (s.d.))	64.2 (7.7)
Male	21,303 (48.5)
Body mass index, kg/m^2 (mean (s.d.))	26.5 (4.4)
Hypertension	13,473 (30.7)
Diabetes mellitus type 2	1,538 (3.5)
Diabetes mellitus type 1	173 (0.4)
Hyperlipidemia	472 (1.1)
Chronic kidney disease	379 (0.9)
Coronary artery disease	2,669 (6.1)
Heart failure	302 (0.7)
Atrial fibrillation	1,346 (3.1)
Cirrhosis	69 (0.2)
Pancreatitis	157 (0.4)
Gastroesophageal reflux disease	5,681 (12.9)
Any malignancy	5,665 (12.9)
Myocardial T1 time, ms (median (IQR))	918.5 (892.8–943.4)
Liver T1 time, ms (median (IQR))	544.0 (514.0–578.0)
Iron-corrected liver T1 time, ms (median (IQR))	693.0 (662.0–730.0)
Pancreas T1 time, ms (median (IQR))	674.0 (624.0–734.0)
Renal cortex T1 time, ms (median (IQR))	1,200.0 (1,150.0–1,252.0)

Values are presented as the number (percentage) unless otherwise specified. A subset of the study sample had data available for each MRI parameter: myocardial T1 (n = 39,339), liver T1 (n = 36,516), iron-corrected liver T1 (n = 28,221), pancreas T1 (n = 33,862) and renal cortex T1 (n = 30,155).

https://doi.org/10.1038/s41591-024-03010-w

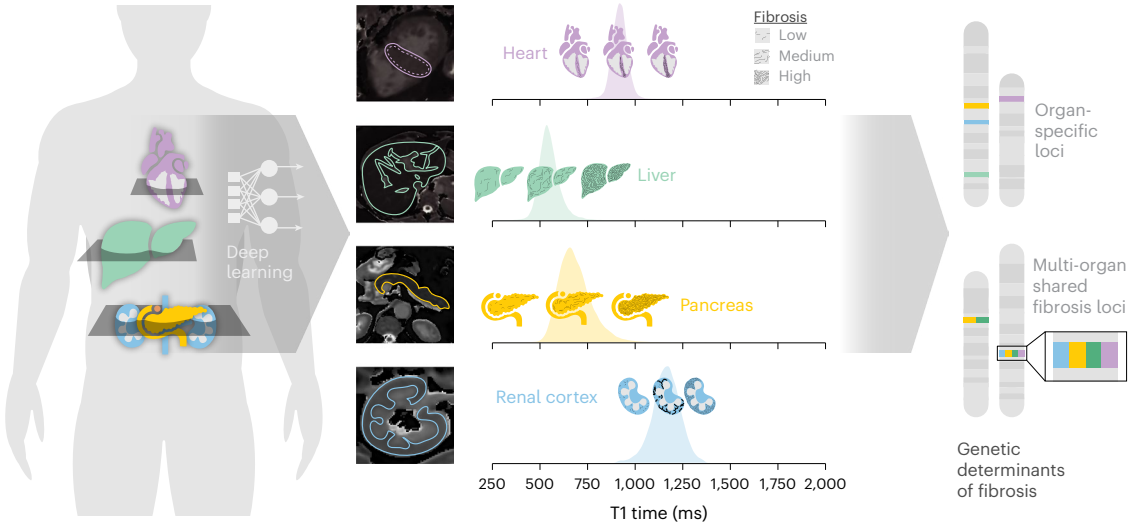

Fig. 1 | Study flow chart. Left, machine learning-based segmentation of the myocardial IVS, liver, pancreas and renal cortex from transverse ShMOLLI T1 maps. Middle, Distribution of measured native T1 time from segmented organs of interest. Higher native T1 time generally reflects a higher burden of fibrosis. Right, Machine learning-derived organ-specific T1 times were examined for organ-specific genetic determinants (upper) and shared genetic determinants (lower). Organ schematics adapted from Servier Medical Art by Servier under a Creative Commons license CC BY 4.0. T1 maps reproduced by kind permission of UK Biobank ©.

$P = 6.45 \times 10^{-14}$) and type 2 diabetes mellitus ($OR_{/s.d.} = 1.20$, 95% CI 1.13–1.28; $P = 1.23 \times 10^{-8}$; Fig. 2a and Supplementary Table 4).

T1 time and cardiac, metabolic and fibrotic diseases

Next, we examined the association of a priori selected prevalent cardiovascular, metabolic and fibrotic diseases with change in T1 time (Methods). The results are summarized in Fig. 2b and Supplementary Table 5. Two-sided P values < 5.6×10^{-3} were considered statistically significant.

Briefly, we found that chronic kidney disease was associated with increased T1 times in the renal cortex, liver and heart with the largest increase seen in renal cortex T1 time ($\Delta T1_{renal\ cortex}$ (s.d.) = 0.34, 95% CI 0.23–0.45; $P = 5.72 \times 10^{-9}$). Type 1 and 2 diabetes mellitus were associated with increased T1 time in the heart. Higher pancreas T1 time was noted among participants with type 1 diabetes mellitus ($\Delta T1_{pancreas}$ (s.d.) = 0.52, 95% CI 0.36–0.69; $P = 7.78 \times 10^{-10}$) but not those with type 2 diabetes mellitus ($\Delta T1_{pancreas}$ (s.d.) = 0.05, 95% CI −0.01 to 0.10; $P = 0.08$) at time of MRI. Type 2 diabetes mellitus, however, was associated with increased T1 time in the liver ($\Delta T1_{liver}$ (s.d.) = 0.53, 95% CI 0.47–0.58; $P = 1.81 \times 10^{-83}$) and renal cortex ($\Delta T1_{renal\ cortex}$ (s.d.) = 0.17, 95% CI 0.11–0.23; $P = 6.03 \times 10^{-8}$). As expected, given the central role of fibrosis in the pathogenesis of cirrhosis, liver cirrhosis was associated with a sizable increase in liver T1 time ($\Delta T1_{liver}$ (s.d.) = 0.60, 95% CI 0.35–0.84; $P = 1.43 \times 10^{-6}$). Prior history of pancreatitis was associated with both higher liver and pancreas T1 time. Heart failure was associated with higher T1 time in the heart and liver. Hypertension was associated with an increase in T1 time in the renal cortex and liver. The lack of association of hypertension in the absence of concomitant left ventricular hypertrophy with increased myocardial T1 time has been previously described[8]. Finally, we found a significant association of hyperlipidemia and coronary artery disease with increased liver T1 time.

Biomarker associations of T1 time mirror its link to disease

Biomarker associations with T1 time were consistent with the association of T1 time with diseases that are tagged by the respective biomarkers (Supplementary Fig. 11 and Supplementary Table 6). For instance, increased liver T1 time was associated with increased levels of circulating aspartate aminotransferase and alanine aminotransferase, markers of liver injury and gamma glutamyl transferase and alkaline phosphatase, markers of hepatobiliary pathology. Estimated glomerular filtration rate (eGFR) calculated using the Chronic Kidney Disease-Epidemiology Collaboration (CKD-EPI) equation incorporating both cystatin C and creatinine[9] had an inverse relationship with renal cortex T1 time, highlighting the association of increased renal fibrosis with impaired renal function. Urine microalbuminuria, which is linked to glomerulosclerosis and abnormal glomerular permeability[10], was associated with increased renal cortex T1 time. Urinary sodium excretion, which is tightly correlated with hypertension and sodium intake[11], was associated with increased T1 time in the renal cortex and liver.

Several biomarkers had consistent associations across multiple organs. Higher hemoglobin A1c and cystatin C were associated with increased T1 in the liver, pancreas, heart and renal cortex. C-reactive protein, a nonspecific marker of systemic inflammation, was associated with increased T1 time in the liver, pancreas and renal cortex. A number of biomarkers were associated with decreased fibrosis across multiple organs. Higher levels of circulating albumin, bilirubin, high-density lipoprotein, apolipoprotein(a) and vitamin D were associated with lower T1 times across multiple organs.

Multi-organ T1 GWAS reveals shared and organ-specific pathways

We next examined the genetic underpinnings of interstitial fibrosis using common variant genome-wide association studies (GWAS). We found that interstitial fibrosis is heritable, albeit to varying degrees across the examined organs. Single nucleotide polymorphism (SNP) heritability (h^2_g) was highest for the liver ($h^2_g = 0.33 \pm 0.02$) and renal cortex T1 time ($h^2_g = 0.31 \pm 0.02$) followed by pancreas T1 time ($h^2_g = 0.21 \pm 0.02$). Myocardial T1 time was associated with the lowest heritability among the examined organs ($h^2_g = 0.13 \pm 0.01$). We identified 27, 18, 11 and 10 independent genetic loci associated with liver, pancreas, myocardial and renal cortex T1 time, respectively (Fig. 3a–d and Supplementary Tables 7–10). There was no evidence of inflation in our GWAS results (Fig. 3e and Supplementary Table 11). Regional association plots for genome-wide significant variants are shown in Supplementary Figs. 12–15.

Liver T1 time GWAS. Of the 27 identified independent genome-wide significant loci in the liver T1 GWAS, 17 are new and 10 have been previously reported to be associated with liver T1 time (Fig. 3a, Supplementary Table 7 and Supplementary Fig. 12)[12,13]. Among the new variants, 4

variants tagged human leukocyte antigen genes (*HLA-A*, *HLA-B*, *HLA-E* and *HLA-DQA1*). *HLA* genes have been previously shown to be important contributors to autoimmune liver disease risk[14–16]. The new variants include the intronic variant rs201081507_G ($P = 1.28 \times 10^{-68}$) in *BANK1*, with roles implicated in B cell activity and systemic autoimmune disorders[17]. *MANBA/NFKB1* and *CYP21A2*, which are implicated in autoimmune primary biliary cholangitis[18,19] and liver fibrosis[20], were among the genes tagged by the lead variants rs34406062_A ($P = 5.68 \times 10^{-21}$) and rs6467_C ($P = 2.17 \times 10^{-9}$), respectively.

Missense variant rs1800562_A ($P = 1.38 \times 10^{-126}$) in *HFE*, which accounts for the majority of cases of hereditary hemochromatosis, was among the variants most significantly associated with liver T1 time[21]. Additionally, variants tagging *H2BC11* (rs13191659_G, $P = 3.50 \times 10^{-55}$) and *H2BC13* (rs142175606_AT, $P = 7.84 \times 10^{-49}$), with roles in hepatic iron homeostasis, were implicated in our results[22].

The short indel chr6: 28436135_AAC_A ($P = 5.10 \times 10^{-41}$) in close proximity to *GPX6*, which encodes glutathione peroxidase-6 and plays a central role in protection against cellular oxidative stress and liver fibrosis[23], was among the identified lead variants. The remaining genome-wide significant variants mapped in proximity to genes associated with liver cirrhosis[24], hepatocellular carcinoma[25] and type 2 diabetes mellitus[26], including *MTARC1*, *CENPE* and *CARMIL1*, respectively.

In a conditional analysis adjusting for lead variants within each identified locus, 6 additional independent genome-wide significant variants were identified, of which 3 mapped to new genes including *ZNF322*, *IFI30* and *HNRNPUL1* (Supplementary Table 12 and Supplementary Fig. 16). *IFI30* encodes gamma-interferon-inducible lysosomal thiol reductase and has previously been associated with nonalcoholic fatty liver disease[27–29]. *HNRNPUL1* has been associated with alcohol-induced liver cirrhosis via regulation of *TGFB1* expression in hepatocytes[24].

Given the central role of the liver in iron metabolism and storage[30] and the paramagnetic properties of iron that influence T1 time[31], we performed a sensitivity GWAS of iron-corrected liver T1 time to examine the genetic determinants of T1 time independent of liver iron content. Of the 36,516 participants with liver T1 time in this study, 28,221 had iron-corrected liver T1 time available in the UKB under field ID 40062 (ref. 13). Genetic correlation between liver T1 and iron-corrected liver T1 time was high ($r_g = 0.99 \pm 0.02$). We identified 17 genome-wide significant loci associated with iron-corrected liver T1 time, of which 16 overlapped with the main liver T1 time GWAS loci (Supplementary Table 13 and Supplementary Fig. 17). rs116783737_A ($P = 3.98 \times 10^{-8}$) in close proximity to *TACR3* was the lead variant in the nonoverlapping locus. Loci implicated in iron homeostasis including *HFE/SLC17A2, TMPRSS6, H2BC13* and *H2AC12/H2BC11* remained associated with iron-corrected liver T1 time; however, the association was attenuated as compared to liver T1 time.

Pancreas T1 time GWAS. In the pancreas T1 time GWAS, 18 independent new genome-wide significant loci were identified (Fig. 3b, Supplementary Table 8 and Supplementary Fig. 13). Several of these loci have been previously reported to associate with measures of pancreatic volume (*PROX1*, *ABO* and *CTRB2*) and fat (*FAF1*, *ABO* and *CEBPB*) in the UKB[22]. The top genome-wide significant variant, rs13107325_T, is a missense variant within *SLC39A8* and associated with increased pancreas T1 time ($P = 2.44 \times 10^{-33}$). The short indel chr16: 75234273_CTTT_C falling in an intergenic region near *CTRB1/CTRB2* was the second lead variant associated with pancreas T1 time ($P = 5.05 \times 10^{-26}$). *CTRB1/CTRB2* encode pancreatic proteolytic enzymes chymotrypsinogen A/B and have been recently implicated in a GWAS of chronic pancreatitis[32].

Lead variants tagging nearest genes *ABO* (rs782134971_GAAACTGCC_G, $P = 4.80 \times 10^{-19}$) and *FUT2* (rs2548458_C, $P = 1.70 \times 10^{-22}$), two genes found to be associated with lipase activity and chronic pancreatitis[33], were among the genome-wide significant variants. Additionally, two loci defined by their nearest gene implicate *PROX1* (rs7555143_T, $P = 2.78 \times 10^{-9}$) and *KLB* (rs71643295_C_CAGGGTTT, $P = 1.84 \times 10^{-8}$), which have important roles in pancreatic exocrine development[34] and proteostasis[35]. Lead variants tagging nearest genes associated with pancreatic endocrine function including *RREB1* (ref. 36; rs2842895_G, $P = 6.34 \times 10^{-11}$), *CEBPB*[37,38] (rs2094716_C, $P = 1.32 \times 10^{-10}$) and *KLB*[39] (rs71643295_C_CAGGGTTT, $P = 1.84 \times 10^{-8}$) were also among the identified loci highlighting the role of pancreatic fibrosis in islet cell function.

Several lead variants associated with pancreas T1 time mapped close to genes implicated in cell cycle regulation, fibrosis and pancreatic cancer including *SLC41A1* (ref. 40), *TLK1* (ref. 41), *SORBS2* (ref. 42), *RREB1* (ref. 43), *GXYLT1* (ref. 44) and *CEBPB*[45]. Additionally, lead variants rs573197054_C ($P = 2.79 \times 10^{-9}$) and rs7287124_G ($P = 1.23 \times 10^{-15}$) tagging *CRELD2* and *XBP1*, respectively, which have been shown to be central to the endoplasmic stress response, were among the implicated loci[46,47]. Activation of the endoplasmic stress response and increased expression of *XBP1* has been reported in patients with chronic pancreatitis[48].

In a conditional analysis, one additional independent genome-wide significant variant was identified, which mapped to the previously identified *CTRB1/CTRB2* region in the main pancreas T1 time GWAS (Supplementary Table 14 and Supplementary Fig. 18).

Heart T1 time GWAS. In the heart T1 time GWAS, we recently described 11 independent loci (Fig. 3c, Supplementary Table 9 and Supplementary Fig. 14)[8]. Briefly, the identified loci implicated genes involved in glucose transport (*SLC2A12*), iron homeostasis (*HFE* and *TMPRSS6*), tissue repair (*ADAMTSL1* and *VEGFC*), oxidative stress (*SOD2*), cardiac hypertrophy (*MYH7B*) and calcium signaling (*CAMK2D*)[8]. In a conditional analysis, no additional new variants were identified.

Renal cortex T1 time GWAS. In the renal cortex T1 time GWAS, 10 independent genome-wide significant loci were identified (Fig. 3d, Supplementary Table 10 and Supplementary Fig. 15). The top variant associated with renal cortex T1 time was rs10157011_A ($P = 3.17 \times 10^{-181}$), which fell within the *DNAJC16/CASP9/CELA2B* locus on chromosome 1 that has been reproducibly associated with renal function in genetic association studies[49–51]. Previous studies examining this locus on chromosome 1 using integrative genetic analysis, single-nuclear epigenome mapping and CRISPR–Cas9 gene editing prioritized *CASP9* over *DNAJC16* and *CELA2B* as the likely causal gene. *CASP9* encodes a cysteine-aspartic protease that is integral to autophagy and apoptosis, and increased

Fig. 2 | Multi-organ T1 time association with disease. a, Circular plot depicting phenome-wide associations of liver, pancreas, heart and renal cortex T1 time. Multiple logistic regression was implemented adjusting for age at MRI, body mass index, sex and MRI scanner. Two-sided *P* value $< 4 \times 10^{-5}$ was used to define phenome-wide significant associations after adjusting for multiple testing. The *y* axis represents $-\log_{10}(P \text{ value})$ for each examined association. The *y* axis was curtailed at $-\log_{10}(P \text{ value}) = 20$ for the liver T1 phenome-wide association results. $^*P < 1 \times 10^{-20}$. Labels on outer spokes represent parent phecodes with phenome-wide significant associations. Upward-facing triangles reflect an increased odds of disease associated with increased organ-specific T1 time. Downward-facing triangles reflect a decreased odds of disease associated with increased organ-specific T1 time. **b**, Multivariable-adjusted changes in multi-organ T1 times associated with select diseases. Multiple linear regression was implemented adjusting for age at MRI, body mass index, sex and MRI scanner. Triangle colors represent the respective organ T1 times examined as labeled in the legend. Triangle size represents the magnitude of change in T1 time associated with a particular disease as represented in the legend. Two-sided *P* value $< 5.6 \times 10^{-3}$ (0.05/9) was used to define statistically significant associations after adjusting for multiple testing. Filled triangles represent associations with two-sided *P* value $< 5.6 \times 10^{-3}$, and empty triangles represent associations with two-sided *P* value $\geq 5.6 \times 10^{-3}$. Derm., dermatologic; Heme, hematopoietic; IDs, infectious diseases; Inj. & Pois., injuries and poisonings; NEC, not elsewhere classified; Neuro, neurologic; NOS, not otherwise specified; Obst., obstetrics; Cong., congenital anomalies; Symp., symptoms.

https://doi.org/10.1038/s41591-024-03010-w

CASP9 expression is associated with kidney disease[52]. rs10157011_A is associated with decreased expression of *CASP9* in cultured human fibroblasts (Supplementary Fig. 19) and lower renal cortex T1 time and fibrosis in our study.

Concordant with findings from the liver and pancreas, the missense variant rs13107325_T in *SLC39A8* was among the top genome-wide significant variants associated with increased renal cortex T1 time ($P = 1.62 \times 10^{-162}$).

rs201081507_G, an intronic variant in the *BANK1* gene, which encodes a B cell-specific scaffold protein and has been previously associated with systemic lupus erythematosus[53] and lupus nephritis[54], was implicated in our results ($P = 5.80 \times 10^{-51}$). *PPP3CA*, which

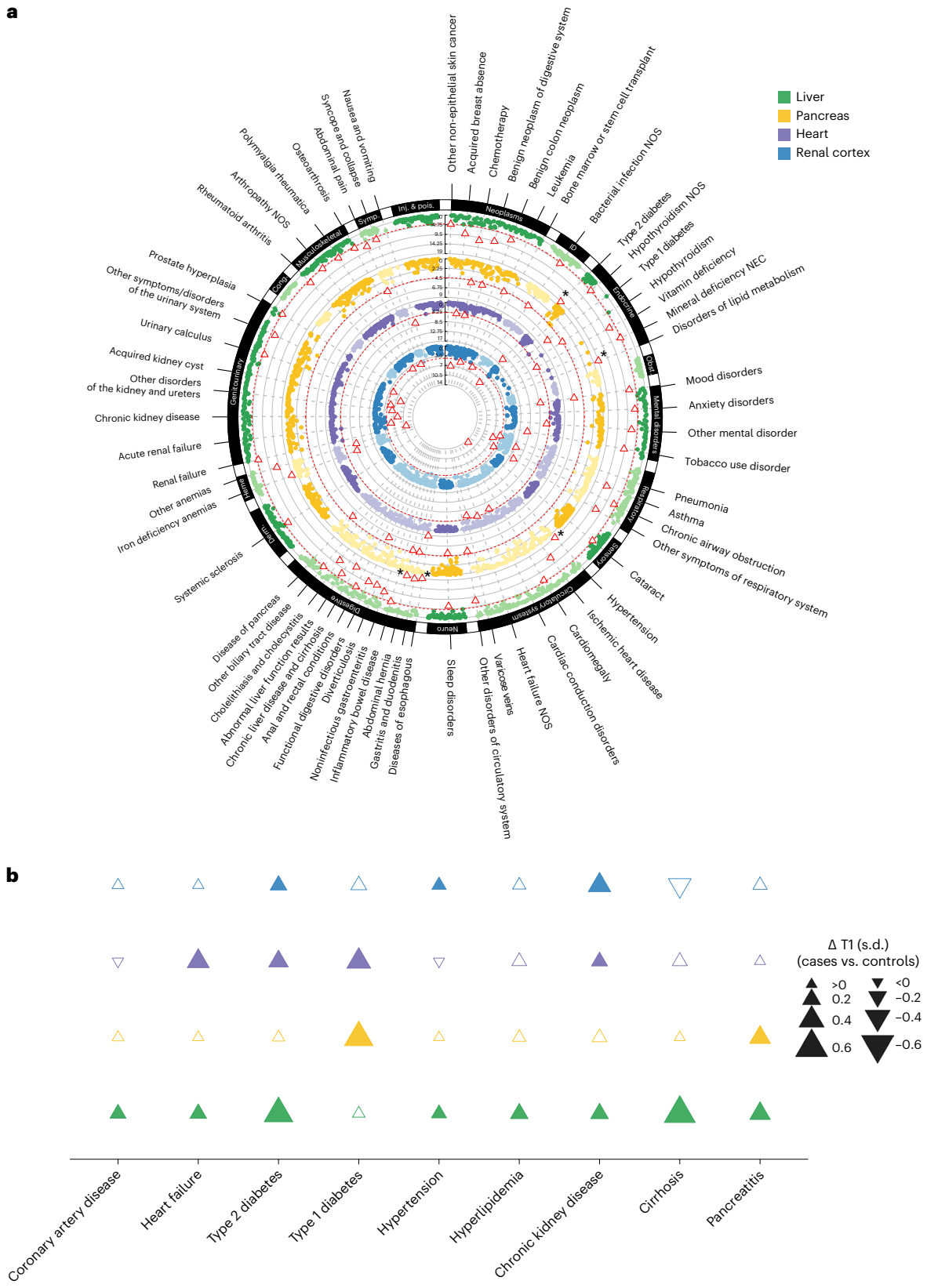

https://doi.org/10.1038/s41591-024-03010-w

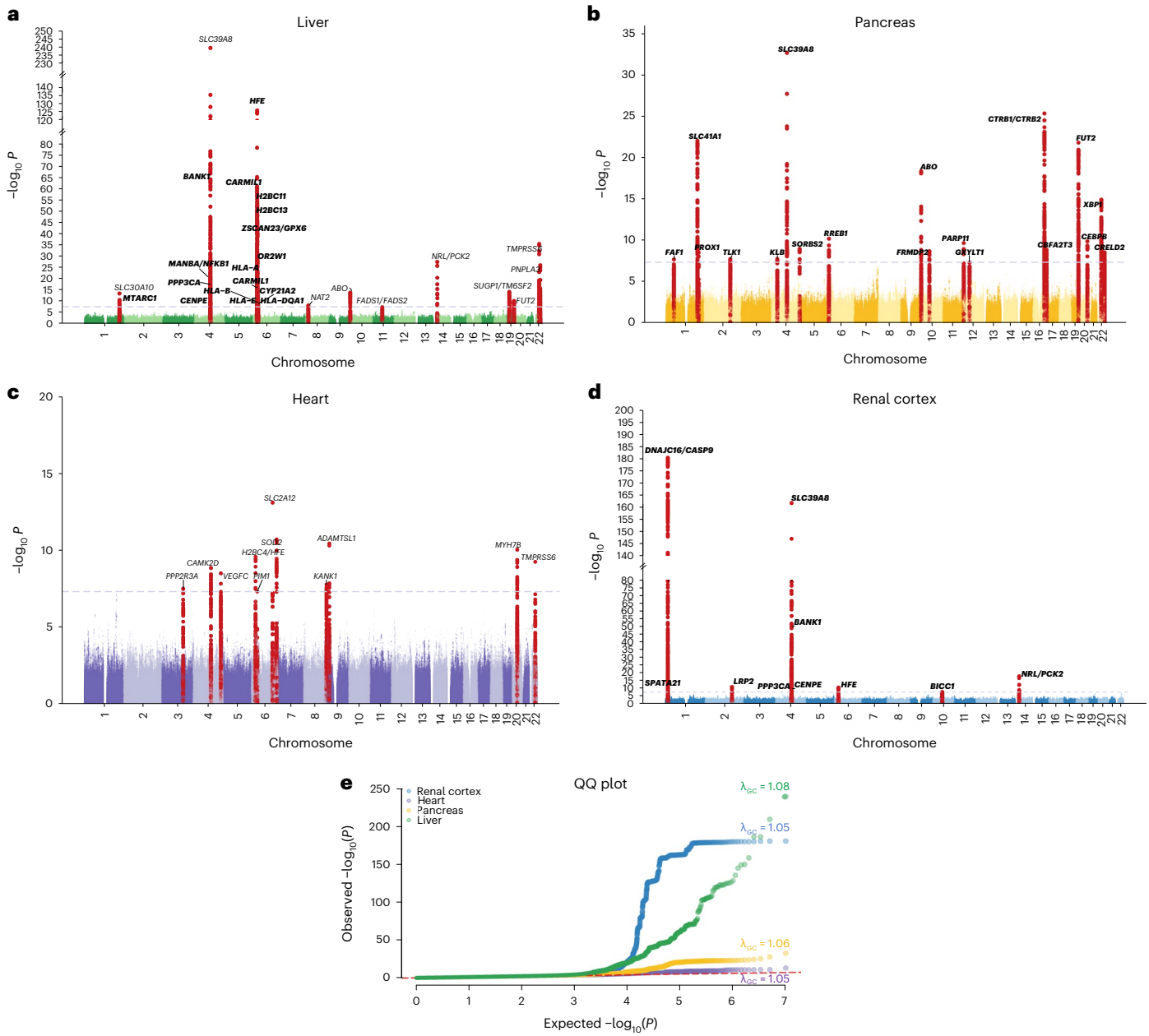

Fig. 3 | Multi-organ T1 time genome-wide association results. a–d, Manhattan plots depicting genome-wide association results across the 22 autosomes for the investigated organs. Fixed-effects multiple linear regression models were implemented. Nearest genes are used for annotation. Bolded gene names reflect new loci. The dashed line represents the threshold for genome-wide significance (two-sided *P* value < 5×10^{-8} adjusted for multiple testing). **e**, Quantile–quantile (QQ) plot for each organ-specific genome-wide association analysis. Two-sided observed and expected *P* values are plotted. Figure 3c depicts previously published genome-wide association results of myocardial T1 time from ref. 8. λ_{GC}, genomic control factor.

encodes the catalytic subunit of calcineurin, was among the identified loci (rs77161209_C, $P = 4.50 \times 10^{-09}$). Calcineurin plays integral roles in T cell activation[55], and immunosuppressive calcineurin inhibitors are known to be associated with nephrotoxicity and renal fibrosis[56].

Another intronic variant, rs16856530_T, within *LRP2* was associated with renal cortex T1 time ($P = 1.14 \times 10^{-11}$) and previously reported in genetic association studies of GFR[57]. Pathogenic variants in *LRP2* are associated with the autosomal recessive Donnai-Barrow/facio-oculo-acoustico-renal (DB/FOAR) syndrome characterized by glomerular proteinuria and progression to chronic kidney disease[58]. Recently, low-density lipoprotein receptor-related 2 (LRP2) was identified as a target antigen in acquired anti-brush border antibody disease, an aggressive form of primary renal tubulointerstitial disease[59]. The RNA-binding protein Bicaudal-C1, associated with cystic renal disease[60], was among the identified loci tagged by the intronic short indel rs35079883_CT_C within *BICC1*.

In a sensitivity GWAS analysis adjusting for eGFR, 9 of 10 independent loci identified in the main GWAS remained genome-wide significant (Supplementary Table 15).

In a conditional analysis of renal cortex T1 time, three additional independent genome-wide significant variants were identified, which mapped to nearest genes *CELA2B/CASP9*, *SLC39A8* and *H2BC3/HFE*, that were previously identified in the primary renal cortex T1 time GWAS (Supplementary Table 16 and Supplementary Fig. 20).

Multi-organ T1 time shared loci. The pleiotropic associations of genome-wide significant loci across the examined organs are summarized in Fig. 4a–d and Supplementary Table 17. Notably, one locus that mapped to the nearest gene *SLC39A8* was associated with increased fibrosis across all three abdominal organs. The locus defined by the nearest gene *HFE* was associated with decreased liver, heart and renal cortex T1 time, likely a reflection of iron tissue deposition, which alters tissue magnetic properties and is associated with lower T1 time[61]. Additional shared loci among the examined organs included: *PPP3CA*, *BANK1*, *NRL/PCK2*, *MANBA/NFKB1* and *CENPE* in the liver and renal cortex; *ABO* and *FUT2* in the liver and pancreas; and *TMPRSS6* in the liver and heart. Overall, the genetic correlation of T1 time was modest across the examined organs (Fig. 4e). Genetic correlation was highest between the liver and renal cortex T1 time ($r_g = 0.44 \pm 0.15$).

Cell-type-specific expression of multi-organ T1 GWAS loci

Next, we evaluated the putative biologic roles of the identified organ-specific T1 time loci from each organ bed. To that end, we sought to identify for each organ the cell type(s) responsible for expressing the nearest genes associated with genome-wide significant loci using publicly available single-cell RNA sequencing (scRNA-seq) and/or single-nucleus RNA sequencing (snRNA-seq)[62–65]. To quantify cell-type-specific enrichment of these genes within each organ, we constructed a gene module for each organ, consisting of nearest genes for all organ-specific T1 time GWAS loci, and scored each cell type for expression of this module.

For the liver, many of the immune cell clusters produced the greatest liver module scores, while stellate cells scored relatively low (Supplementary Fig. 21a–c). The highest pancreas module scores were derived from acinar cell types. Additionally, macrophages and stellate cells did show signs of enrichment, despite representing a small population of the overall cell composition of the pancreas (Supplementary Fig. 21d–f). Cardiomyocytes and endocardial cells (endothelial II) showed the highest cardiac module scores (Supplementary Fig. 22a–c). Finally in the kidney, proximal tubule cells and parietal epithelial cells were among the top-scoring clusters (Supplementary Fig. 22d–f). Overall, our results demonstrate that the identified multi-organ T1 time loci include both fibroblast-specific and non-fibroblast-specific signals and suggest that many T1-associated genetic signals likely operate in a cell-nonautonomous manner to promote organ-wide fibrosis.

Burden of multi-organ fibrosis associated with mortality

Lastly, we examined the impact of the burden of multi-organ fibrosis on all-cause mortality among 23,293 study participants with complete T1 time data for the liver, pancreas, heart and renal cortex over a median follow-up of 1.87 years (IQR 1.20–2.75 years). Study participants were stratified into the lower 80th and upper 20th percentiles of T1 time for each organ. We devised a simple, and easy-to-remember, scoring system, where we assign one point per organ if its T1 time falls in the upper 20th percentile of T1 times for that organ. We found a significant trend of increased mortality with an increasing number of organs (0 versus 1–2 versus 3–4) with a T1 time in the upper 20th percentile (log-rank P value $= 3.0 \times 10^{-7}$) (Fig. 5a). In multivariable analysis, individuals with a high burden of fibrosis in ≥3 organs, as defined above, had a 3.31-fold-increased risk of all-cause mortality compared to individuals with no organs with T1 time in the top 20th percentile (hazard ratio (HR) = 3.31, 95% CI 1.77–6.19; $P = 1.78 \times 10^{-4}$; Fig. 5b).

Discussion

We leveraged machine learning to conduct a large-scale, multi-organ study of interstitial fibrosis, measured using T1 mapping, in approximately 44,000 individuals in the UKB. In contrast to prior studies of T1 mapping that focus on specific fibrotic diseases and are restricted to analysis of T1 time in a single organ, our study examines the distribution of T1 time across multiple organs in the general population and establishes reference ranges for T1 time in the liver, pancreas, renal cortex and heart. In a PheWAS, we demonstrate the association of organ-specific T1 time with diseases across multiple organ systems and highlight the multi-organ involvement with fibrosis associated with several prevalent metabolic, cardiovascular and fibrotic diseases in the population. Furthermore, we demonstrate that noninvasive assessment of interstitial fibrosis across multiple organs using T1 mapping enables risk stratification of all-cause mortality in the population. In our multi-organ genetic association analyses, we identify 58 independent genomic loci associated with T1 time, many of which were new including 17 in the liver, 18 in the pancreas and 10 in the renal cortex. Overall, the inter-organ genetic correlation of T1 time was modest. Several loci overlapped across the examined organs implicating genes involved in myriad biologic pathways including metal ion transport (*SLC39A8*, *HFE* and *TMPRSS6*), glucose metabolism (*PCK2*), blood group antigens (*ABO* and *FUT2*), immune function (*BANK1* and *PPP3CA*), inflammation (*NFKB1*) and mitosis (*CENPE*).

Our findings have several important implications. First, we demonstrate the feasibility of automated quantification of T1 time across multiple organs at scale. T1 mapping of the pancreas[66] and kidney[67] have not been thoroughly examined in the literature and, in contrast to liver[68] and heart[69] T1 mapping, are not part of routine clinical imaging protocols for evaluation of diseases of the pancreas and kidney, respectively.

Exocrine diseases of the pancreas including pancreatitis and functional digestive disorders were associated with elevated pancreas T1 time. This is in line with prior small studies suggesting a role for pancreas T1 mapping in the early diagnosis and follow-up of individuals with chronic pancreatitis[4] and pancreatic exocrine insufficiency[70]. Interestingly, type 1 but not type 2 diabetes mellitus was associated with increased pancreas T1 time, which may reflect the autoimmune destruction of islet cells and ensuing fibrotic changes associated with type 1 diabetes mellitus. Up to 15% of individuals with new-onset diabetes are misclassified and incorrectly treated despite contemporary diagnostic testing[71]. Further studies are needed to evaluate the potential role of pancreas T1 mapping as a diagnostic adjunct for classification of diabetes mellitus and monitoring disease progression in type 1 diabetes mellitus.

Higher renal cortex T1 time was associated with chronic kidney disease, lower GFR and higher microalbuminuria, hence confirming the correlation between structural changes captured by T1 mapping and kidney function reported in prior smaller studies[67]. Our study establishes reference ranges for renal cortex T1 time in the population and promises to enhance our understanding of variation in renal cortex T1 time in health and disease states.

Second, we identified several shared genomic loci associated with fibrosis in multiple organs. The missense variant rs13107325_T (p.Ala391Thr) within *SLC39A8* was among the top genome-wide significant variants associated with increased T1 time in the liver, pancreas and renal cortex. The variant rs13107325_T is highly pleiotropic[72]. *SLC39A8* encodes the ZIP8 metal cation transporter of manganese, which is an important cofactor for several enzymes including superoxide dismutase and glycosyltransferases[73]. Homozygous loss-of-function mutations in *SLC39A8* are associated with type 2 congenital disorder of glycosylation and Leigh syndrome[74]. Carriers of rs13107325_T have decreased ZIP8 function and demonstrate low serum manganese and deficiencies in glycosylation[75,76]. Interestingly, we found no association between rs13107325_T and myocardial T1 time. A knock-in mouse model of rs13107325_T demonstrated a significant reduction in manganese levels in the liver and kidney but no impact on manganese levels in the heart[77]. These findings suggest that the association of rs13107325_T with interstitial fibrosis may be related to manganese levels; however, this was not directly tested in our study.

https://doi.org/10.1038/s41591-024-03010-w

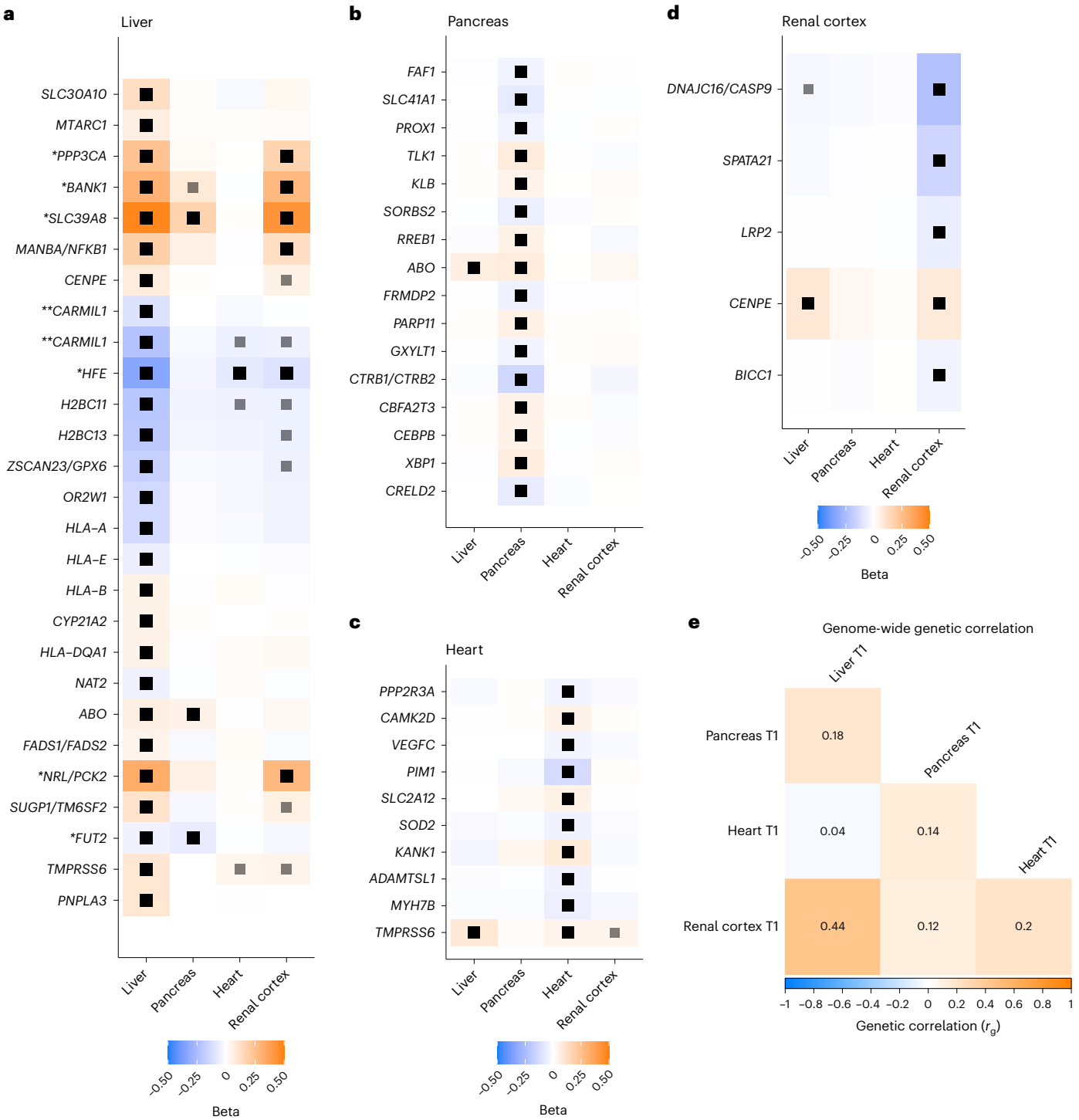

Fig. 4 | Genetic correlation of multi-organ T1 time. a–d, Association of organ-specific genome-wide significant lead variants within genome-wide significant loci defined by nearest gene with T1 time across multiple organs. Fixed-effect multiple linear regression models were implemented. Loci are arranged by increasing chromosome number and chromosome position. Large black rectangles reflect genome-wide significant associations (two-sided *P* value $< 5 \times 10^{-8}$) after adjusting for multiple testing. Small gray rectangles reflect associations with $5 \times 10^{-8} \leq$ two-sided *P* value $< 5 \times 10^{-4}$. *Loci with lead variants that overlap across organs or are in high linkage disequilibrium ($R^2 > 0.8$) are reported once. Lead variants tagging overlapping loci across organs and that are not in high linkage disequilibrium ($R^2 < 0.8$) are reported separately. **Two lead SNPs in the liver T1 GWAS nearest to *CARMIL1* (rs72826361_C and rs75580845_C) are in linkage equilibrium ($R^2 = 0.13$) and are hence reported separately (top, rs72826361_C; bottom, rs75580845_C). **e**, Genome-wide genetic correlation matrix of T1 time across multiple organs.

An intronic variant rs201081507_G in *BANK1* was associated with increased T1 time in the liver and renal cortex T1 time GWASs and was a subthreshold variant in the pancreas T1 time GWAS ($P = 8.14 \times 10^{-7}$). *BANK1* has been implicated in B cell signaling and autoimmune systemic disorders associated with multi-organ inflammation and fibrosis including lupus nephritis, inflammatory bowel disease and primary sclerosing cholangitis[17,54,78]. Additionally, *NFKB1* and *PPP3CA* with integral roles in inflammation[79] and immune regulation[55] were among the

https://doi.org/10.1038/s41591-024-03010-w

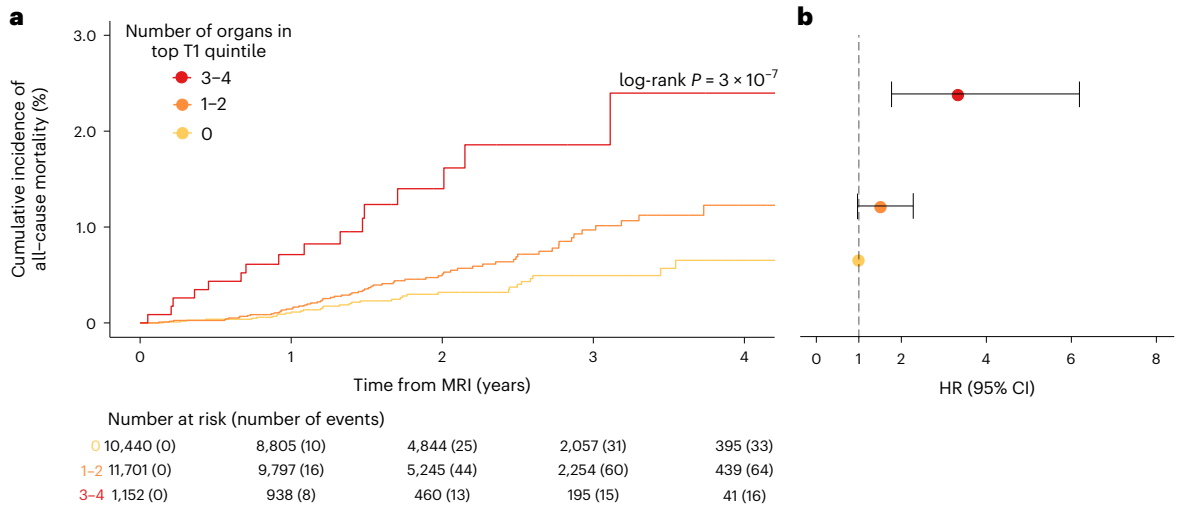

Fig. 5 | All-cause mortality stratified by number of organs with T1 time in the top quintile. a, Kaplan–Meier plot of all-cause mortality stratified by number of organs (0, 1–2 or 3–4) among the examined organs including liver, pancreas, heart and kidneys with T1 time in the top quintile. Log-rank test was used to assess the trend of all-cause mortality with increasing burden of multi-organ fibrosis. Two-sided *P* value < 0.05 was considered statistically significant. **b**, Forest plot depicting multivariable-adjusted HR of all-cause mortality associated with increasing number of organs (1–2, *n* = 11,701; 3–4, *n* = 1,152) with organ-specific T1 time in the top quintile. The referent group (*n* = 10,440) comprised participants with organ-specific T1 times of the liver, pancreas, heart and kidneys that fell within the lower 80th percentile of the study sample distribution. The dots represent multivariable-adjusted HRs, and the error bars reflect the associated 95% CI. Multivariable Cox proportional-hazards model was implemented adjusting for age, sex, body mass index, MRI scanner, coronary artery disease, heart failure, atrial fibrillation, type 1 diabetes mellitus, type 2 diabetes mellitus, hypertension, hyperlipidemia, chronic kidney disease, cirrhosis, pancreatitis and history of malignancy. Two-sided *P* value < 0.05 was considered statistically significant.

shared loci between liver and renal cortex T1 time. Our findings are in line with mouse models that demonstrate progressive chronic inflammation, premature aging and decreased liver regenerative potential with *Nfkb1* knockout[80].

ABO and *FUT2*, two genes responsible for determining blood group type and expression of the ABO antigens in body secretions, respectively, were among the shared loci associated with pancreas and liver T1 time. The *ABO–FUT2* genotype, and epistasis, has been associated with susceptibility to infections[81], autoimmune disorders[82], pancreatitis[33] and pancreatic cancer[83]. Further interrogation of the role of the identified shared loci in fibrosis is needed and may have wide-ranging implications for several fibrotic diseases.

Despite the several identified shared genome-wide significant T1 time loci in our study, the overall genetic correlation of T1 time across organs was modest. This may reflect that the uncovered genetic signal associated with T1 time in each organ is influenced by both disease states/pathologic insults associated with fibrosis in that organ, as well as shared tissue fibrosis pathways.

Third, our results highlight several new organ-specific loci associated with interstitial fibrosis and implicated in fibrotic diseases associated with a substantial burden on public health. In the liver, we identified several loci implicated in alcohol-induced[24] (*MTARC1* and *HNRNPUL1)* and non-alcohol-induced[28,84] (*MTARC1 and IFI30*) liver cirrhosis. In the pancreas, we confirm the association of the intergenic region between *CTRB1* and *CTRB2*, previously reported to modulate risk of alcohol-induced and non-alcohol-induced pancreatitis, in pancreatic fibrosis[32]. In the kidney, we provide evidence supporting the role of *CASP9* in renal fibrosis and progression of CKD[52]. Lead variant rs10157011_A is associated with decreased expression of *CASP9* in cultured human fibroblasts and is associated with decreased renal cortex interstitial fibrosis in our study. This is congruent with findings from mouse studies where genetic deletion or pharmacological inhibition of CASP9 showed decreased apoptosis, improved autophagy and protection from acute kidney injury and renal fibrosis[52]. Small molecules that inhibit CASP9 have been developed[85] and thus our study extends findings from mouse studies and prioritizes CASP9 as a potential therapeutic target for renal fibrosis.

Finally, noninvasive assessment of interstitial fibrosis across multiple organs enables risk stratification of all-cause mortality in the population even after accounting for a comprehensive list of demographic factors and comorbidities. Given the intimate association between pathological aging and fibrosis[86–88], multi-organ assessment of interstitial fibrosis may serve as a surrogate for biological age. These findings may suggest a role for T1 mapping in screening for individuals at high-risk for adverse prognosis and emphasize the critical need to understand the pathways contributing to fibrosis to improve population health.

Our study has several limitations. First, our choice of examined organs was dictated by the T1 mapping sequences available as part of the UKB MRI protocol. Examination of interstitial fibrosis in other organs is needed to fully unravel the complexity of the biologic processes underlying fibrosis in the human body. Second, T1 maps for each organ in the UKB are obtained at a single slice which may not be representative of interstitial fibrosis throughout the examined organ. Third, kidney T1 time was measured in a subset of pancreas T1 maps that included cross-sections of the kidney and not from dedicated kidney T1 maps, which (1) may have introduced bias, and (2) prohibited adequate sampling of the renal medulla and assessment of renal medulla T1 time, which has important implications for renal function and disease. Fourth, T1 mapping is a valuable tool for noninvasive assessment of tissue characteristics; however, a number of limitations impact T1 mapping as a surrogate for interstitial fibrosis including potential confounding factors such as inflammation, edema, paramagnetic ions and variability across imaging sequences. Other MRI techniques such as liver magnetic resonance elastography, which has been demonstrated to outperform T1 mapping in staging of liver fibrosis, were not accessible for examination in this study[89]. Fifth, UKB participants are predominantly of European ancestry and findings from our genetic analysis should be replicated in multi-ancestry cohorts.

In conclusion, multi-organ interstitial fibrosis is associated with morbidity and mortality. T1 mapping allows for noninvasive assessment of interstitial fibrosis in multiple organs and is of prognostic value in risk stratification of all-cause mortality in the population. By leveraging

machine learning, we quantified T1 time across multiple organs at scale and provided new insights into organ-specific and shared biologic pathways underlying fibrosis for further interrogation.

Online content

Any methods, additional references, Nature Portfolio reporting summaries, source data, extended data, supplementary information, acknowledgements, peer review information; details of author contributions and competing interests; and statements of data and code availability are available at https://doi.org/10.1038/s41591-024-03010-w.

References

1. Wynn, T. A. Fibrotic disease and the T_H1/T_H2 paradigm. *Nat. Rev. Immunol.* **4**, 583–594 (2004).
2. Chen, Y. et al. Aging reprograms the hematopoietic-vascular niche to impede regeneration and promote fibrosis. *Cell Metab.* **33**, 395–410 (2021).
3. Banerjee, R. et al. Multiparametric magnetic resonance for the non-invasive diagnosis of liver disease. *J. Hepatol.* **60**, 69–77 (2014).
4. Cheng, M. et al. T1 mapping for the diagnosis of early chronic pancreatitis: correlation with Cambridge classification system. *Br. J. Radiol.* **94**, 20200685 (2021).
5. Diao, K. et al. Histologic validation of myocardial fibrosis measured by T1 mapping: a systematic review and meta-analysis. *J. Cardiovasc. Magn. Reson.* **18**, 92 (2017).
6. Mao, W. et al. Evaluation of interstitial fibrosis in chronic kidney disease by multiparametric functional MRI and histopathologic analysis. *Eur. Radiol.* **33**, 4138–4147 (2023).
7. Dekkers, I. A. et al. Consensus-based technical recommendations for clinical translation of renal T1 and T2 mapping MRI. *MAGMA* **33**, 163–176 (2020).
8. Nauffal, V. et al. Genetics of myocardial interstitial fibrosis in the human heart and association with disease. *Nat. Genet.* **55**, 777–786 (2023).
9. Inker, L. A. et al. Estimating glomerular filtration rate from serum creatinine and cystatin C. *N. Engl. J. Med.* **367**, 20–29 (2012).
10. Marre, M., Bouhanick, B. & Berrut, G. Microalbuminuria. *Curr. Opin. Nephrol. Hypertens.* **3**, 558–563 (1994).
11. Welsh, C. E. et al. Urinary sodium excretion, blood pressure, and risk of future cardiovascular disease and mortality in subjects without prior cardiovascular disease. *Hypertension* **73**, 1202–1209 (2019).
12. O'Dushlaine, C. et al. Genome-wide association study of liver fat, iron, and extracellular fluid fraction in the UK Biobank. Preprint at *medRxiv* https://doi.org/10.1101/2021.10.25.21265127 (2021).
13. Parisinos, C. A. et al. Genome-wide and Mendelian randomisation studies of liver MRI yield insights into the pathogenesis of steatohepatitis. *J Hepatol.* **73**, 241–251 (2020).
14. Karlsen, T. H. & Chung, B. K. Genetic risk and the development of autoimmune liver disease. *Dig. Dis.* **33**, 13–24 (2015).
15. Donaldson, P. T. Genetics of liver disease: immunogenetics and disease pathogenesis. *Gut* **53**, 599–608 (2004).
16. Mack, C. L. HLA Associations in pediatric autoimmune liver diseases: current state and future research initiatives. *Front. Immunol.* **13**, 1019339 (2022).
17. Ellinghaus, D. et al. Analysis of five chronic inflammatory diseases identifies 27 new associations and highlights disease-specific patterns at shared loci. *Nat. Genet.* **48**, 510–518 (2016).
18. Hitomi, Y. et al. NFKB1 and MANBA confer disease susceptibility to primary biliary cholangitis via independent putative primary functional variants. *Cell Mol. Gastroenterol. Hepatol.* **7**, 515–532 (2019).
19. Ueno, K. et al. Integrated GWAS and mRNA microarray analysis identified IFNG and CD40L as the central upstream regulators in primary biliary cholangitis. *Hepatol. Commun.* **4**, 724–738 (2020).
20. Luedde, T. & Schwabe, R. F. NF-κB in the liver–linking injury, fibrosis and hepatocellular carcinoma. *Nat. Rev. Gastroenterol. Hepatol.* **8**, 108–118 (2011).
21. Pilling, L. C. et al. Common conditions associated with hereditary haemochromatosis genetic variants: cohort study in UK Biobank. *BMJ* **364**, k5222 (2019).
22. Liu, Y. et al. Genetic architecture of 11 organ traits derived from abdominal MRI using deep learning. *Elife* **10**, e65554 (2021).
23. Ramos-Tovar, E. & Muriel, P. Molecular mechanisms that link oxidative stress, inflammation, and fibrosis in the liver. *Antioxidants* **9**, 1279 (2020).
24. Innes, H. et al. Genome-wide association study for alcohol-related cirrhosis identifies risk loci in *MARC1* and *HNRNPUL1*. *Gastroenterology* **159**, 1276–1289 (2020).
25. He, P. et al. Reduced expression of CENP-E contributes to the development of hepatocellular carcinoma and is associated with adverse clinical features. *Biomed. Pharmacother.* **123**, 109795 (2020).
26. Chen, J. et al. The trans-ancestral genomic architecture of glycemic traits. *Nat. Genet.* **53**, 840–860 (2021).
27. Vujkovic, M. et al. A multiancestry genome-wide association study of unexplained chronic ALT elevation as a proxy for nonalcoholic fatty liver disease with histological and radiological validation. *Nat. Genet.* **54**, 761–771 (2022).
28. Subudhi, S. et al. Distinct hepatic gene-expression patterns of NAFLD in patients with obesity. *Hepatol Commun* **6**, 77–89 (2022).
29. Haas, M. E. et al. Machine learning enables new insights into genetic contributions to liver fat accumulation. *Cell Genom.* **1**, 100066 (2021).
30. Kohgo, Y., Ikuta, K., Ohtake, T., Torimoto, Y. & Kato, J. Body iron metabolism and pathophysiology of iron overload. *Int. J. Hematol.* **88**, 7–15 (2008).
31. Mojtahed, A. et al. Reference range of liver corrected T1 values in a population at low risk for fatty liver disease-a UK Biobank sub-study, with an appendix of interesting cases. *Abdom. Radiol.* **44**, 72–84 (2019).
32. Rosendahl, J. et al. Genome-wide association study identifies inversion in the *CTRB1-CTRB2* locus to modify risk for alcoholic and non-alcoholic chronic pancreatitis. *Gut* **67**, 1855–1863 (2018).
33. Weiss, F. U. et al. Fucosyltransferase 2 (FUT2) non-secretor status and blood group B are associated with elevated serum lipase activity in asymptomatic subjects, and an increased risk for chronic pancreatitis: a genetic association study. *Gut* **64**, 646–656 (2015).
34. Westmoreland, J. J. et al. Pancreas-specific deletion of Prox1 affects development and disrupts homeostasis of the exocrine pancreas. *Gastroenterology* **142**, 999–1009 (2012).
35. Hernandez, G. et al. Pancreatitis is an FGF21-deficient state that is corrected by replacement therapy. *Sci. Transl. Med.* **12**, eaay5186 (2020).
36. Mattis, K. K. et al. Loss of *RREB1* in pancreatic beta cells reduces cellular insulin content and affects endocrine cell gene expression. *Diabetologia* https://doi.org/10.1007/s00125-022-05856-6 (2022).
37. Matsuda, T. et al. Ablation of C/EBPβ alleviates ER stress and pancreatic beta cell failure through the GRP78 chaperone in mice. *J. Clin. Invest.* **120**, 115–126 (2010).
38. Aksit, M. A. et al. Pleiotropic modifiers of age-related diabetes and neonatal intestinal obstruction in cystic fibrosis. *Am. J. Hum. Genet.* **109**, 1894–1908 (2022).
39. Geng, L. et al. β-Klotho promotes glycolysis and glucose-stimulated insulin secretion via GP130. *Nat. Metab.* **4**, 608–626 (2022).

40. Xie, J. et al. Magnesium transporter protein solute carrier family 41 member 1 suppresses human pancreatic ductal adenocarcinoma through magnesium-dependent Akt/mTOR inhibition and bax-associated mitochondrial apoptosis. *Aging* **11**, 2681–2698 (2019).
41. Kim, J.-A. et al. Comprehensive functional analysis of the tousled-like kinase 2 frequently amplified in aggressive luminal breast cancers. *Nat. Commun.* **7**, 12991 (2016).
42. Jie, R., Zhu, P., Zhong, J., Zhang, Y. & Wu, H. LncRNA KCNQ1OT1 affects cell proliferation, apoptosis and fibrosis through regulating miR-18b-5p/SORBS2 axis and NF-κB pathway in diabetic nephropathy. *Diabetol. Metab. Syndr.* **12**, 77 (2020).
43. Su, J. et al. TGF-β orchestrates fibrogenic and developmental EMTs via the RAS effector RREB1. *Nature* **577**, 566–571 (2020).
44. Peng, L. et al. A stop-gain mutation in *GXYLT1* promotes metastasis of colorectal cancer via the MAPK pathway. *Cell Death Dis.* **13**, 395 (2022).
45. Cheng, P. et al. Menin coordinates C/EBPβ-mediated TGF-β signaling for epithelial-mesenchymal transition and growth inhibition in pancreatic cancer. *Mol. Ther. Nucleic Acids* **18**, 155–165 (2019).
46. Waldron, R. T. et al. Ethanol induced disordering of pancreatic acinar cell endoplasmic reticulum: an ER stress/defective unfolded protein response model. *Cell Mol. Gastroenterol. Hepatol.* **5**, 479–497 (2018).
47. Hartley, T. et al. Endoplasmic reticulum stress response in an INS-1 pancreatic beta-cell line with inducible expression of a folding-deficient proinsulin. *BMC Cell Biol.* **11**, 59 (2010).
48. Zhou, L. et al. ATF6 regulates the development of chronic pancreatitis by inducing p53-mediated apoptosis. *Cell Death Dis.* **10**, 662 (2019).
49. Pattaro, C. et al. Genetic associations at 53 loci highlight cell types and biological pathways relevant for kidney function. *Nat. Commun.* **7**, 10023 (2016).
50. Morris, A. P. et al. Trans-ethnic kidney function association study reveals putative causal genes and effects on kidney-specific disease aetiologies. *Nat. Commun.* **10**, 29 (2019).
51. Hellwege, J. N. et al. Mapping eGFR loci to the renal transcriptome and phenome in the VA Million Veteran Program. *Nat. Commun.* **10**, 3842 (2019).
52. Doke, T. et al. Genome-wide association studies identify the role of caspase-9 in kidney disease. *Sci. Adv.* **7**, eabi8051 (2021).
53. Gómez Hernández, G., Morell, M. & Alarcón-Riquelme, M. E. The role of BANK1 in B cell signaling and disease. *Cells* **10**, 1184 (2021).
54. Bolin, K. et al. Variants in BANK1 are associated with lupus nephritis of European ancestry. *Genes Immun.* **22**, 194–202 (2021).
55. Dutta, D. et al. Recruitment of calcineurin to the TCR positively regulates T cell activation. *Nat. Immunol.* **18**, 196–204 (2017).
56. Ume, A. C., Wenegieme, T.-Y. & Williams, C. R. Calcineurin inhibitors: a double-edged sword. *Am. J. Physiol. Renal Physiol.* **320**, F336–F341 (2021).
57. Liu, H. et al. Epigenomic and transcriptomic analyses define core cell types, genes and targetable mechanisms for kidney disease. *Nat. Genet.* **54**, 950–962 (2022).
58. Charlton, J. R. et al. Beyond the tubule: pathological variants of LRP2, encoding the megalin receptor, result in glomerular loss and early progressive chronic kidney disease. *Am. J. Physiol. Renal Physiol.* **319**, F988–F999 (2020).
59. Larsen, C. P. et al. LDL receptor-related protein 2 (Megalin) as a target antigen in human kidney anti-brush border antibody disease. *J. Am. Soc. Nephrol.* **29**, 644–653 (2018).
60. Rothé, B., Gagnieux, C., Leal-Esteban, L. C. & Constam, D. B. Role of the RNA-binding protein Bicaudal-C1 and interacting factors in cystic kidney diseases. *Cell. Signal.* **68**, 109499 (2020).
61. Stark, D. D. et al. Magnetic resonance imaging and spectroscopy of hepatic iron overload. *Radiology* **154**, 137–142 (1985).
62. Andrews, T. S. et al. Single-cell, single-nucleus, and spatial RNA sequencing of the human liver identifies cholangiocyte and mesenchymal heterogeneity. *Hepatol. Commun.* **6**, 821–840 (2022).
63. Tosti, L. et al. Single-nucleus and in situ RNA-sequencing reveal cell topographies in the human pancreas. *Gastroenterology* **160**, 1330–1344 (2021).
64. Simonson, B. et al. Single-nucleus RNA sequencing in ischemic cardiomyopathy reveals common transcriptional profile underlying end-stage heart failure. *Cell Rep.* **42**, 112086 (2023).
65. Quatredeniers, M. et al. Meta-analysis of single-cell and single-nucleus transcriptomics reveals kidney cell type consensus signatures. *Sci. Data* **10**, 361 (2023).
66. Serrao, E. M. et al. Magnetic resonance fingerprinting of the pancreas at 1.5 T and 3.0 T. *Sci. Rep.* **10**, 17563 (2020).
67. Wolf, M. et al. Magnetic resonance imaging T1- and T2-mapping to assess renal structure and function: a systematic review and statement paper. *Nephrol. Dial. Transplant.* **33**, ii41–ii50 (2018).
68. Yoon, J. H., Lee, J. M., Paek, M., Han, J. K. & Choi, B. I. Quantitative assessment of hepatic function: modified look-locker inversion recovery (MOLLI) sequence for T1 mapping on Gd-EOB-DTPA-enhanced liver MR imaging. *Eur. Radiol.* **26**, 1775–1782 (2016).
69. Messroghli, D. R. et al. Clinical recommendations for cardiovascular magnetic resonance mapping of T1, T2, T2* and extracellular volume: a consensus statement by the Society for Cardiovascular Magnetic Resonance (SCMR) endorsed by the European Association for Cardiovascular Imaging (EACVI). *J. Cardiovasc. Magn. Reson.* **19**, 75 (2017).
70. Ashihara, N. et al. Correlation of pancreatic T1 values using modified look-locker inversion recovery sequence (MOLLI) with pancreatic exocrine and endocrine function. *J. Clin. Med.* **9**, 1805 (2020).
71. Farmer, A. & Fox, R. Diagnosis, classification, and treatment of diabetes. *BMJ* **342**, d3319 (2011).
72. Pickrell, J. K. et al. Detection and interpretation of shared genetic influences on 42 human traits. *Nat. Genet.* **48**, 709–717 (2016).
73. Nebert, D. W. & Liu, Z. *SLC39A8* gene encoding a metal ion transporter: discovery and bench to bedside. *Hum. Genomics* **13**, 51 (2019).
74. Choi, E. -K., Nguyen, T. -T., Gupta, N., Iwase, S. & Seo, Y. A. Functional analysis of *SLC39A8* mutations and their implications for manganese deficiency and mitochondrial disorders. *Sci. Rep.* **8**, 3163 (2018).
75. Mealer, R. G. et al. The schizophrenia risk locus in *SLC39A8* alters brain metal transport and plasma glycosylation. *Sci. Rep.* **10**, 13162 (2020).
76. Lin, W. et al. Hepatic metal ion transporter ZIP8 regulates manganese homeostasis and manganese-dependent enzyme activity. *J. Clin. Invest.* **127**, 2407–2417 (2017).
77. Sunuwar, L. et al. Pleiotropic ZIP8 A391T implicates abnormal manganese homeostasis in complex human disease. *JCI Insight* **5**, e140978 (2020).
78. Kozyrev, S. V. et al. Functional variants in the B-cell gene *BANK1* are associated with systemic lupus erythematosus. *Nat. Genet.* **40**, 211–216 (2008).
79. Liu, T., Zhang, L., Joo, D. & Sun, S.-C. NF-κB signaling in inflammation. *Signal. Transduct. Target Ther.* **2**, 17023 (2017).
80. Jurk, D. et al. Chronic inflammation induces telomere dysfunction and accelerates ageing in mice. *Nat. Commun.* **2**, 4172 (2014).
81. Ahluwalia, T. S. et al. *FUT2–ABO* epistasis increases the risk of early childhood asthma and *Streptococcus pneumoniae* respiratory illnesses. *Nat. Commun.* **11**, 6398 (2020).

82. Ye, B. D. et al. Association of *FUT2* and *ABO* with Crohn's disease in Koreans. *J. Gastroenterol. Hepatol.* **35**, 104–109 (2020).
83. Wolpin, B. M. et al. Variant *ABO* blood group alleles, secretor status, and risk of pancreatic cancer: results from the pancreatic cancer cohort consortium. *Cancer Epidemiol. Biomarkers Prev.* **19**, 3140–3149 (2010).
84. Lewis, L. C. et al. Hepatocyte mARC1 promotes fatty liver disease. *JHEP Rep.* https://doi.org/10.1016/j.jhepr.2023.100693 (2023).
85. Ozoren, N. et al. The caspase 9 inhibitor Z-LEHD-FMK protects human liver cells while permitting death of cancer cells exposed to tumor necrosis factor-related apoptosis-inducing ligand. *Cancer Res.* **60**, 6259–6265 (2000).
86. Kanasaki, K., Kitada, M. & Koya, D. Pathophysiology of the aging kidney and therapeutic interventions. *Hypertens. Res.* **35**, 1121–1128 (2012).
87. Gazoti Debessa, C. R., Mesiano Maifrino, L. B. & Rodrigues de Souza, R. Age related changes of the collagen network of the human heart. *Mech. Ageing Dev.* **122**, 1049–1058 (2001).
88. Hunt, N. J., (Sophie Kang, S. W., Lockwood, G. P., Le Couteur, D. G. & Cogger, V. C. Hallmarks of aging in the liver. *Comput. Struct. Biotechnol. J.* **17**, 1151–1161 (2019).
89. von Ulmenstein, S. et al. Assessment of hepatic fibrosis and inflammation with look-locker T1 mapping and magnetic resonance elastography with histopathology as reference standard. *Abdom. Radiol.* **47**, 3746–3757 (2022).

Publisher's note Springer Nature remains neutral with regard to jurisdictional claims in published maps and institutional affiliations.

Springer Nature or its licensor (e.g. a society or other partner) holds exclusive rights to this article under a publishing agreement with the author(s) or other rightsholder(s); author self-archiving of the accepted manuscript version of this article is solely governed by the terms of such publishing agreement and applicable law.

© The Author(s), under exclusive licence to Springer Nature America, Inc. 2024

Victor Nauffal[1,2,12], Marcus D. R. Klarqvist[3,12], Matthew C. Hill[2,11], Danielle F. Pace[2,3], Paolo Di Achille[3], Seung Hoan Choi[2], Joel T. Rämö[2], James P. Pirruccello[2,4,5], Pulkit Singh[3], Shinwan Kany[2,6], Cody Hou[2], Kenney Ng[7], Anthony A. Philippakis[2,3,8], Puneet Batra[3], Steven A. Lubitz[9] & Patrick T. Ellinor[2,9,10] ✉

[1]Cardiovascular Division, Brigham and Women's Hospital, Boston, MA, USA. [2]Cardiovascular Disease Initiative, Broad Institute of MIT and Harvard, Cambridge, MA, USA. [3]Data Sciences Platform, Broad Institute of MIT and Harvard, Cambridge, MA, USA. [4]Cardiology Division, Massachusetts General Hospital, Boston, MA, USA. [5]Division of Cardiology, University of California, San Francisco, San Francisco, CA, USA. [6]Department of Cardiology, University Heart and Vascular Center Hamburg-Eppendorf, Hamburg, Germany. [7]Center for Computational Health, IBM Research, Cambridge, MA, USA. [8]Eric and Wendy Schmidt Center, Broad Institute of MIT and Harvard, Cambridge, MA, USA. [9]Demoulas Center for Cardiac Arrhythmias, Massachusetts General Hospital, Boston, MA, USA. [10]Cardiovascular Research Center, Massachusetts General Hospital, Boston, MA, USA. [11]Present address: Cardiovascular Research Center, Massachusetts General Hospital, Boston, MA, USA. [12]These authors contributed equally: Victor Nauffal, Marcus. D. R. Klarqvist. ✉e-mail: ellinor@mgh.harvard.edu

Methods

To summarize, we trained machine learning models to segment the liver, pancreas and kidney T1 maps from the UKB to measure organ-specific T1 times. For the heart, we recently reported myocardial T1 time in the same study participants[8]. We performed a PheWAS of organ-specific T1 time. We then examined the association of organ-specific T1 time with select prevalent diseases at time of MRI as well as with baseline serum and urine biomarkers. We then performed genome-wide association analyses of organ-specific T1 times and examined the shared and organ-specific genetic determinants of fibrosis. Using publicly available scRNA-seq and snRNA-seq data, we examined cell-type-specific expression of multi-organ T1 time GWAS loci. Lastly, we assessed the association of multi-organ interstitial fibrosis burden with all-cause mortality during follow-up.

Study design and population

The UKB is a prospective cohort of 502,629 individuals from the UK enrolled between 2006 and 2010 with deep phenotyping, imaging and multiple genomic data types. The cohort design has been previously described[90–92]. Briefly, around 9.2 million individuals aged 40–69 years living in England, Scotland and Wales were invited to participate in the study, and 5.4% agreed to participate. Extensive questionnaire data, physical measures and biologic samples were collected at baseline, with ongoing data collection in large subsets of the cohort, including repeated assessments and multimodal imaging. Starting in 2014, UKB participants were invited to return for the first multimodal imaging visit including MRI with T1 mapping of the liver, pancreas, kidneys and heart allowing for the assessment of interstitial fibrosis in these organs. As of January 2022, 43,881 UKB participants had both imputed genetic data and T1 mapping data available. All study participants are followed longitudinally for health-related outcomes through linkage to national health-related datasets.

Analysis on UKB data was performed under application number 7089 and was approved by the local Massachusetts General Hospital institutional review board (IRB). UKB data are made available to researchers from research institutions with genuine research inquiries, following IRB and UKB approval. Genome-wide association analysis summary statistics from our study are available for public access ('Data availability').

MRI T1 mapping protocol

A standardized non-contrast enhanced MRI protocol using a clinical wide-bore 1.5 Tesla scanner (MAGNETOM Aera, Syngo Platform VD13A, Siemens Healthcare) was performed on all MRI sub-study participants[92]. The MRI protocol included a brain (30 min), heart (20 min) and abdominal (10 min) MRI sequence. Native T1 mapping within a single breath hold of the liver, pancreas and heart using the cardiac-gated ShMOLLI (WIP780B) technique was performed. In 2019, the UKB added a dedicated ShMOLLI kidney T1 mapping sequence. At the time of this study in January 2022, only 1,893 dedicated kidney T1 maps were available for analysis. The liver T1 mapping sequence was performed in a transverse orientation at the level of the porta hepatis. The pancreas T1 mapping sequence was acquired in a transverse orientation centered at the level of the pancreas. The following imaging parameters for liver and pancreas T1 mapping were implemented: voxel size, $1.146 \times 1.146 \times 8.0\ mm^3$; flip angle, 35 degrees; TE/TR, 1.93/480.6 ms; and R = 2 (ref. 92). The kidney T1 mapping sequence was acquired in the coronal orientation and centered at the level of the kidneys. The cardiac T1 mapping protocol has been described previously[8,93]. Data for the T1 mapping acquisitions were provided as one real-valued, two-dimensional pre-computed T1 map per participant for each of the liver, pancreas, kidneys and heart.

To date, the UKB MRI core laboratory has only released raw T1 maps to UKB researchers. As such, we developed our own automated pipeline to measure T1 times from raw T1 maps. First, we set up an automatic procedure to identify raw T1 map series among the several files provided by the UKB under the category 'shMOLLI' (UKB field IDs: 20204, 20259, 20243 and 20214). Preliminary explorations indicated that the T1 map series names contained the keyword 't1map'. Therefore, we discarded all series with names not containing either of the two keywords. If there was more than one acquisition for that participant, we chose to use the acquisition with the highest median image intensity.

Measurement of liver T1 time

We have previously reported segmentations of the liver from the UKB ShMOLLI sequences[29]. In short, these automated segmentations, with pixels belonging to the liver, were identified using a multi-thresholding approach across the proton density fat fraction and T1 parametric maps for each participant. After Gaussian smoothing, low pixel values in the proton density fat fraction map were identified by Li thresholding[94], leaving pixels comprising the liver, as well as other relatively low-fat regions such as the spleen. To measure liver parenchymal T1 time, we excluded prominent hepatic vasculature and biliary ducts from the liver regions of interest. To this end, segmentation masks derived from the liver ShMOLLI sequence were intersected with the liver T1 maps, leaving only pixels in the T1 map located in the liver. Next, these pixels were then partitioned into low-intensity and high-intensity groups by Otsu thresholding[95]. The lower-intensity pixels represent bona fide parenchymal liver tissue of interest, and the higher-intensity pixels correspond to non-parenchymal structures including hepatic vasculature and biliary ducts. Finally, the segmentation masks were shrunk by morphological erosion to remove any artificial 'halo' effects, followed by removal of all but the largest connected component. T1 times were then derived from the remaining pixels within the final segmented liver region of interest. To obtain a summary measure of liver parenchymal T1 time per participant, we calculated the median T1 time for all pixels within the corresponding liver region of interest (Fig. 1). We validated the results of the machine learning-derived liver T1 time to those measured by experienced physicians in a hold-out validation set ($n = 50$) and found excellent concordance ($r = 0.94$, 95% CI 0.88–0.97; $P = 1.25 \times 10^{-17}$; Supplementary Fig. 3).

Segmentation and measurement of pancreas and kidney T1 time

Axial pancreas T1 maps in the UKB frequently included cross-sections of the right or left kidney (Supplementary Fig. 23). We leveraged these incidental observations to measure kidney T1 time in a larger number of participants ($n = 30{,}155$) compared to those who underwent kidney-dedicated T1 mapping ($n = 1{,}893$). In the axial plane view, only the renal cortex, and not the renal medulla, was well represented and as such we were limited to measurement of renal cortex T1 time in this study.

To develop machine learning models to segment the pancreas and kidneys in this view, we randomly selected 150 (100 training, 50 validation) pancreas T1 maps. An experienced physician (V.N.) labeled the pancreas, liver, kidneys and spine within the axial pancreas T1 maps ($n = 150$). Fifty overlapping images in the training set were independently manually labeled by both V.N. and J.T.R. to allow for inter-reader reproducibility assessment of our manual segmentation method. The manual tracing procedure, called semantic segmentation, displayed high inter-reader concordance between the labeled segmentations, as measured in 50 overlapping MRI acquisitions (Sørensen–Dice (Dice) coefficient for pancreas = 0.83, 95% CI = 0.80–0.85 and for kidneys Dice = 0.90, 95% CI 0.87–0.93). Pixel intensity values were transformed to T1 times using the accompanying T1 map legend for each manually segmented region of interest. T1 times were highly correlated between the two readers (for pancreas, $r = 0.93$, 95% CI 0.86–0.96; $P = 9.00 \times 10^{-19}$; for renal cortex, $r = 0.97$, 95% CI 0.95–0.99; $P = 4.05 \times 10^{-25}$; Supplementary Figs. 24 and 25).

The physician-derived manual labels of pancreas T1 maps served as the ground truth for training our machine learning models to segment the pancreas and kidneys in this view. To generate machine learning

models to segment the relevant organ structures in the pancreas T1 maps, we used the ResNet-34 model[96] as the base encoder model in a U-Net architecture[97] that was pretrained on ImageNet[98]. By leveraging a preexisting large-scale model as the encoder, we are able to use considerably less training data by restricting training to the decoder while keeping the weights of the pretrained encoder frozen. Since the MRI acquisitions are all captured in grayscale, and ImageNet-based models require three channel inputs, we copied the MRI acquisition three times along the z axis resulting in a final shape of 384 × 288 × 3. The models were trained using the Adam optimizer[99] with a learning rate set to a cosine decay policy decaying from 0.001 to 0 over 50 epochs, weight decay of 0.0001, categorical cross-entropy as the loss function, and a batch size of 16. No additional hyperparameter search or ablation studies were performed. For all training data, the following augmentations (random permutations of the training images) were applied: random shifts in the X–Y plane by up to ±16 pixels and rotations by up to ±5 degrees around its center axis.

Auto-segmentation of the pancreas captured the full pancreas including the head, body and tail. No further post-processing was performed. Pancreas T1 time was measured as the median T1 time of all pixels within the segmented pancreas. We found a high correlation between manually derived and machine learning model-derived pancreas T1 time (r = 0.93, 95% CI 0.87–0.96; $P = 1.45 \times 10^{-20}$) in our validation set (n = 50; Supplementary Fig. 4).

To assign anatomic locations for the kidneys, we used the spine segmentation as a central marker of the body, defined as the midpoint of the left-most and right-most extreme pixel locations. Kidney segmentations were then categorized as mapping to either the left or the right of this centerline. To reduce noisy segmentations, we discarded connected components with <200 pixels in total. In cases where there was >1 kidney segment per unilateral kidney, for example, if the segmentation of the right or left kidney is broken in half, we chose the largest segment.

In this work, we are focused on the functional tissue of the kidney, the renal parenchyma, comprising the medulla and cortex. To this end, we removed the renal pelvis, which has considerably higher T1 times compared to the parenchyma, by filtering out pixels in the kidney segmentations with a T1 time in the top 5th percentile. Next, since there is a stark contrast in T1 times between organs and the enclosing body, we frequently observed a 'halo' of artifactually high T1 times at the organ–body cavity interface. We removed this putative technical artifact by eroding the remaining three pixels in the kidney segmentations. At this point, the kidney parenchyma can be classified into low-intensity and high-intensity T1 times. To this end, we used k-means (k = 2) to systematically classify the pixels as from either renal cortex or medulla in an unbiased fashion. Lastly, we computed the mean, median and number of pixels for each of the classified substructures. In the axial plane view, only the renal cortex, and not the renal medulla, was well represented. Because of this, we limited our segmentation to the renal cortex. Pixels from both the right and left renal cortex were pooled, and renal cortex T1 time was measured as the median T1 time of all pixels within the segmented renal cortex. In a hold-out validation set (n = 50), we found high correlation between manually derived and machine learning model-derived renal cortex T1 time in the axial pancreas T1 maps (r = 0.99, 95% CI 0.98–1; $P = 7.70 \times 10^{-59}$; Supplementary Fig. 5).

To ensure the robustness of our measurement of renal cortex T1 time using the axial pancreas T1 maps, we developed a segmentation model, as described above, to quantify renal cortex T1 time using the dedicated coronal T1 mapping sequence that was only available on 1,893 UKB participants. Of the 1,893 participants, 621 also had measurements of renal cortex T1 time from the axial pancreas T1 maps. An experienced physician (V.N.) labeled the kidneys within the coronal kidney T1 maps (n = 100) as training data for our machine learning model. Following segmentation, we applied the same post-processing approach used in the pancreatic view to classify the renal parenchyma as either cortex or medulla. To allow for a granular assessment of renal cortex T1 time correlation, we measured renal cortex T1 time separately for the anatomic right and left renal cortex in the 621 overlapping participants and examined the correlation between T1 times across the two acquisitions (axial and coronal). We found a good correlation between renal cortex T1 time measured in the axial pancreas T1 maps and the coronal kidney T1 maps (r = 0.68, 95% CI 0.65–0.72, $P = 2.61 \times 10^{-111}$; Supplementary Fig. 2).

To further demonstrate that T1 time derived from incidentally captured organs within a T1 map provides a good surrogate for T1 time measured using a dedicated MRI T1 mapping sequence for the respective organ of interest, we developed a machine learning model to segment the liver within the pancreas T1 maps. As described in 'Measurement of liver T1 time', we performed a number of post-processing modifications to exclude the hepatic vasculature and biliary ducts and derive liver parenchymal regions of interest. Liver T1 time was measured as the median T1 time of all pixels within the segmented liver region of interest. We were able to measure liver T1 time in both the liver T1 maps and pancreas T1 maps for 24,009 participants. We found a good correlation between liver T1 time derived from pancreas and liver T1 maps (r = 0.87, 95% CI 0.86–0.88, $P = 1.0 \times 10^{-200}$). This finding further supports our use of renal cortex T1 time measured from axial pancreas T1 maps.

Measurement of myocardial T1 time

We recently reported median mid-myocardial T1 time at the interventricular septum (IVS). The methods behind measurement of myocardial T1 time in the UKB have been previously described[8]. Briefly, two board-certified cardiologists manually labeled multiple cardiac structures including the IVS, left ventricle free wall, papillary muscles, left ventricle blood pool, right ventricle free wall and right ventricle blood pool. For segmenting cardiac structures in cardiac MRI T1 maps, the training was performed identically as described in this work with the exception of using the DenseNet-121 architecture[100] as the base encoder model instead of ResNet-34. To minimize any potential contamination from the residual blood pool, trabeculae or noncardiac structures, we applied a sequence of morphological operations, skeletonization followed by dilation with a three-pixel kernel, to the IVS segment and generated representative mid-myocardial regions of interest within the IVS. In a hold-out validation set (n = 100), we demonstrated high correlation between manually derived and machine learning model-derived myocardial T1 time (r = 0.97, 95% CI 0.95–0.98; $P = 7.61 \times 10^{-60}$; Supplementary Fig. 6).

PheWAS

We performed a PheWAS to examine the association of organ-specific T1 time with diseases and disorders across different organ systems. We defined diseases using v1.2 of Phecode Map[101], which includes a set of 1,867 disease definitions arranged into clinically meaningful groups and identified using standardized sets of International Classification of Disease, 9th and 10th revision codes. Phecode definitions can be found at https://phewascatalog.org/. Diagnostic code sources included hospital data through linkage to national health-related datasets, as well as outpatient general practitioner visit data through linkage to electronic health records. We restricted the association analysis to phecodes with at least ten prevalent cases at the time of MRI. As such, the number of phecodes included in each organ-specific T1 PheWAS varied as follows: liver (n = 1,267), pancreas (n = 1,254), heart (n = 1,285) and renal cortex (n = 1,235). Derived T1 times were rank-based inverse-normal transformed. Multiple logistic regression was implemented to assess the association of organ-specific T1 time with the included phecodes adjusting for age at time of MRI, sex, body mass index and MRI scanner. A two-sided P-value threshold of $<4 \times 10^{-5}$ (0.05/1,285) was considered statistically significant after adjusting for multiple testing.

Association of T1 time with cardiac, metabolic and fibrotic diseases

We then examined the change in T1 time associated with select prevalent metabolic, cardiovascular and fibrotic diseases at time of first visit for MRI. Prevalent clinical diagnoses were ascertained using the International Classification of Diseases, 9th and 10th revisions, codes and Office of Population Censuses and Surveys (OPCS) Classification of Interventions and Procedures version 4 codes as well as self-report (Supplementary Table 18). Examined diseases included coronary artery disease, heart failure, type 1 and 2 diabetes mellitus, hypertension, hyperlipidemia, chronic kidney disease, cirrhosis and pancreatitis. Derived T1 times were rank-based inverse-normal transformed. Multiple linear regression was used to assess the change in organ-specific T1 time associated with prevalent metabolic, cardiovascular and fibrotic diseases at time of MRI adjusting for age at MRI visit, sex, body mass index and MRI scanner. Two-sided P values $< 5.6 \times 10^{-3}$ (0.05/9) were considered statistically significant after adjusting for multiple testing.

Association of biomarkers with T1 time

We leveraged serum and urine biomarker data in the UKB to examine the association of organ-specific T1 time with biomarkers associated with the examined prevalent diseases. Examined serum and urine biomarkers were measured at time of enrollment in the UKB and included lipoproteins, hemoglobin A1c, glucose, insulin-like growth factor 1, albumin, aspartate aminotransferase, alanine aminotransferase, alkaline phosphatase, gamma glutamyl transferase, total bilirubin, direct bilirubin, creatinine, cystatin c, urine microalbumin, urine sodium, C-reactive protein, rheumatoid factor, urate and vitamin D. Biomarker data were available on a subset of participants with organ-specific T1 times (Supplementary Table 6). Biomarkers with skewed distributions, including lipoprotein(a), C-reactive protein, rheumatoid factor, urine microalbumin and gamma glutamyl transferase, were first transformed on the logarithmic scale. All biomarkers were then standardized. Estimated glomerular filtration was calculated using the CKD-EPI equation incorporating both serum creatinine and cystatin C[9]. Multiple linear regression was used to assess the association of biomarkers with organ-specific T1 time further adjusting for age at enrollment, sex, body mass index and MRI scanner. Two-sided P values $< 1.9 \times 10^{-3}$ (0.05/26) were considered statistically significant and $1.9 \times 10^{-3} \leq P$ values < 0.05 were considered borderline significant.

Genotype data, imputation, sample and variant QC

In total, 488,377 UKB participants were genotyped using either one of two overlapping arrays—the UK BiLEVE Axiom Array or the UKB Axiom Array. Before imputation, a number of quality-control (QC) filters were applied to the genotype data. Variants with >5% missing rate, minor allele frequency <0.0001 and that violated Hardy–Weinberg equilibrium (P-value threshold $<1 \times 10^{-12}$) were excluded. Additionally, samples that were identified as outliers for genotype missingness rate (>5%) and heterozygosity were also excluded. These filters resulted in a genotype dataset that included 670,730 autosomal variants in 487,442 samples. Imputation into the Haplotype Reference Consortium and UK10K + 1000 Genomes phase 3 reference panels was carried out using IMPUTE4. The imputation process resulted in a dataset with 93,095,623 autosomal SNPs and short indels in 487,442 individuals[90].

Sample and variant QC filters were applied before conducting genetic association analyses for each organ-specific T1 time, separately. Samples with sex chromosome aneuploidy and those with discordant genetically inferred and self-reported sex were excluded. One of each pair of third-degree relatives or closer was excluded. Variants with imputation quality score (INFO) <0.3 and those with minor allele frequency <0.01 were excluded. Following genomic QC, our dataset included 36,516/37,567 (n post-genomic QC/n pre-genomic QC with T1 time data); 33,862/35,754; 39,339/41,505; and 30,155/31,730 participants with liver, pancreas, heart and renal cortex T1 time, respectively (Supplementary Fig. 1). The number of SNPs and short indels included in each organ-specific T1 time GWAS were: 9,850,430 (liver), 9,856,647 (pancreas), 9,853,972 (heart) and 9,856,061 (renal cortex).

Genome-wide common variant association analysis methods

We performed a common variant genome-wide association analysis of organ-specific T1 times using a fixed-effects linear regression model in PLINK 2.0 (ref. 102). The models were adjusted for age at MRI, sex, MRI scanner, genotyping array and the first ten principal components of genetic ancestry. Rank-based inverse-normal transformation was applied to the measured T1 times from each organ. As such, effect size estimates in the GWAS are dimensionless and reflect approximately multiples of one standard deviation of the underlying quantitative trait. A two-sided P value $< 5 \times 10^{-8}$ was used to define genome-wide significant common variants. Distinct genomic loci were defined by starting with the variant with the lowest P value, excluding other variants within 500 kb, and iterating until no variants remained. The independently significant variants with the lowest P value at each genomic locus are termed lead variants. We then performed a conditional analysis adjusting for the imputed allele dosage of each lead variant to examine for additional independent genome-wide significant variants within a locus. To examine the genetic determinants of liver T1 time independent of liver iron content, we performed a sensitivity genetic association analysis of iron-corrected T1 time provided in the UKB (field ID: 40062)[13] in a subset of the study participants with measured liver T1 time (n = 28,221/36,516). We additionally performed a sensitivity GWAS of renal cortex T1 time adjusting for eGFR to examine the genetic determinants of renal cortex T1 time independent of renal function (n = 28,658/30,155). Linkage disequilibrium (LD) score regression analysis was performed using ldsc version 1.0.0 (ref. 103). With ldsc, the genomic control factor (λ_{GC}) was partitioned into components reflecting polygenicity and inflation, using the software's defaults.

Regional association plots were generated with LocusZoom.js (v5.16.0)[104] using LD data from the 1000G phase 3 European reference panel. In instances where lead SNPs were not part of the 1000G phase 3 reference panel, in-sample LD was calculated using PLINK 1.9.

Heritability and genetic correlation analysis

SNP heritability of organ-specific T1 times were assessed using BOLT-REML (v2.3.4)[105]. We also computed genetic correlation between organ-specific T1 times using LDSC (v1.0.0)[106].

Single-cell analysis

We analyzed four publicly available single-cell datasets[62–65]. All datasets were imported into R and analyzed using Seurat (v4.3.0.1)[107]. To generate modules, the gene lists were input into Seurat's AddModuleScore function. All results were visualized over imported uniform manifold approximation and projection embeddings derived from the original publications.

Association of burden of multi-organ fibrosis with mortality

A time-to-event analysis was performed to assess the association of burden of multi-organ interstitial fibrosis with all-cause mortality. In total, 23,293 participants with complete T1 time data for the liver, pancreas, heart and renal cortex were included. Follow-up time was defined as time from MRI visit to death or last follow-up. We stratified the cohort into the upper 20th and lower 80th percentiles of organ-specific T1 time. We first compared the all-cause mortality HRs associated with the top quintile of T1 time in each organ by fitting a Cox proportional-hazards model including T1 time in all four organs categorized by the upper 20th versus lower 80th percentiles. We found that the HRs (s.e.) associated with the top quintile of T1 time in each organ were overall similar with a marginally higher HR associated with the top quintile of liver T1: $HR_{\text{top quintile of heart T1/lower 4 quintiles}} = 1.48$ (0.21);

$HR_{\text{top quintile of liver T1/lower 4 quintiles}} = 1.89\ (0.20)$; $HR_{\text{top quintile of pancreas T1/lower 4 quintiles}} = 1.47\ (0.21)$; and $HR_{\text{top quintile of kidney cortex T1/lower 4 quintiles}} = 1.44\ (0.22)$. To approximate the burden of multi-organ fibrosis, we devised a simple score where one point was assigned for each organ T1 time value falling in the upper 20th percentile. We additionally generated a score weighted by the all-cause mortality HR associated with the top quintile of T1 time in each organ. We found that the discriminatory power of the simple and weighted score for all-cause mortality was similar (Harrel's C-statistic: weighted score 0.622 and simple score 0.615). As such, we used the simple score in our analysis. Using a multivariable Cox proportional-hazards model adjusted for age at time of MRI, sex, body mass index, MRI scanner, coronary artery disease, heart failure, atrial fibrillation, type 1 diabetes mellitus, type 2 diabetes mellitus, hypertension, hyperlipidemia, chronic kidney disease, cirrhosis, pancreatitis and history of malignancy, we examined the association of increasing burden of multi-organ fibrosis (0 versus 1–2 and 0 versus 3–4 organs with T1 time in the upper 20th percentile) with all-cause mortality. Kaplan–Meier curves were constructed to compare the cumulative incidence of all-cause mortality across groups of increasing burden of multi-organ interstitial fibrosis. The log-rank test was used to test for differences in survival across the examined groups. The validity of the proportional-hazards assumption was verified by examining the Schoenfeld residuals. All statistical tests were performed using R (v4.0.2).

Reporting summary

Further information on research design is available in the Nature Portfolio Reporting Summary linked to this article.

Data availability

UKB data are made available to researchers from research institutions with genuine research inquiries, following IRB and UKB approval. Genome-wide association analysis summary statistics are available from the Downloads page of the Cardiovascular Disease Knowledge Portal (https://cvd.hugeamp.org/). Genome Reference Consortium Human Build 37 (GRCh37) data are publicly available at https://www.ncbi.nlm.nih.gov/assembly/GCF_000001405.13/. Genome Reference Consortium Human Build 38 (GRCh38) data are publicly available at https://www.ncbi.nlm.nih.gov/assembly/GCF_000001405.26/. Single-cell data for each organ are available via: Liver, (Gene Expression Omnibus (GEO) accession number GSE185477); Pancreas, https://doi.org/10.6084/m9.figshare.12173232 (ref. 108); Heart, processed single-cell data are available at https://singlecell.broadinstitute.org/single_cell/study/SCP1849/ and raw sequence data are available for authorized users at the database of Genotypes and Phenotypes, under accession number phs001539.v4.p1; Kidney, https://doi.org/10.6084/m9.figshare.21587670.v1 (ref. 109) (single-cell data) and https://doi.org/10.6084/m9.figshare.21587679.v1 (ref. 110) (single-nucleus data). Source data are provided with this paper. All other data are contained within the article and its supplementary information.

Code availability

Code used to ingest, for QC and to train machine learning models is available at https://github.com/broadinstitute/ml4h under an open-source BSD license.

References

90. Bycroft, C. et al. The UK Biobank resource with deep phenotyping and genomic data. *Nature* **562**, 203–209 (2018).
91. Sudlow, C. et al. UK Biobank: an open access resource for identifying the causes of a wide range of complex diseases of middle and old age. *PLoS Med.* **12**, e1001779 (2015).
92. Littlejohns, T. J. et al. The UK Biobank imaging enhancement of 100,000 participants: rationale, data collection, management and future directions. *Nat. Commun.* **11**, 2624 (2020).
93. Petersen, S. E. et al. UK Biobank's cardiovascular magnetic resonance protocol. *J. Cardiovasc. Magn. Reson.* **18**, 8 (2015).
94. Li, C. H. & Lee, C. K. Minimum cross entropy thresholding. *Pattern Recognit.* **26**, 617–625 (1993).
95. Otsu, N. A threshold selection method from gray-level histograms. *IEEE Trans. Syst. Man Cybern.* **9**, 62–66 (1979).
96. He, K., Zhang, X., Ren, S. & Sun, J. Deep residual learning for image recognition. Preprint at https://arxiv.org/abs/1512.03385 (2015).
97. Ronneberger, O., Fischer, P. & Brox, T. U-Net: convolutional networks for biomedical image segmentation. in *Medical Image Computing and Computer-Assisted Intervention – MICCAI 2015* (eds Navab, N. et al.) vol. 9351, 234–241 (Springer International Publishing, 2015).
98. Deng, J. et al. ImageNet: a large-scale hierarchical image database. in *2009 IEEE Conference on Computer Vision and Pattern Recognition* 248–255 https://doi.org/10.1109/CVPR.2009.5206848 (IEEE, 2009).
99. Kingma, D. P. & Ba, J. Adam: a method for stochastic optimization. Preprint at https://arxiv.org/abs/1412.6980v9 (2017).
100. Huang, G., Liu, Z., Pleiss, G., Maaten, Lvander & Weinberger, K. Q. Convolutional networks with dense connectivity. *IEEE Trans. Pattern Anal. Mach. Intell.* **44**, 8704–8716 (2022).
101. Wu, P. et al. Mapping ICD-10 and ICD-10-CM codes to phecodes: workflow development and initial evaluation. *JMIR Med. Inform.* **7**, e14325 (2019).
102. Chang, C. C. et al. Second-generation PLINK: rising to the challenge of larger and richer datasets. *Gigascience* **4**, 7 (2015).
103. Schizophrenia Working Group of the Psychiatric Genomics Consortium. et al. LD score regression distinguishes confounding from polygenicity in genome-wide association studies. *Nat. Genet.* **47**, 291–295 (2015).
104. Boughton, A. P. et al. LocusZoom.js: interactive and embeddable visualization of genetic association study results. *Bioinformatics* https://doi.org/10.1093/bioinformatics/btab186 (2021).
105. Loh, P.-R. et al. Contrasting genetic architectures of schizophrenia and other complex diseases using fast variance-components analysis. *Nat. Genet.* **47**, 1385–1392 (2015).
106. Bulik-Sullivan, B. et al. An atlas of genetic correlations across human diseases and traits. *Nat. Genet.* **47**, 1236–1241 (2015).
107. Hao, Y. et al. Integrated analysis of multimodal single-cell data. *Cell* **184**, 3573–3587 (2021).
108. Tosti, L et al. In situ RNA sequencing of the juvenile, adult and diseased pancreas. Figshare. https://doi.org/10.6084/m9.figshare.12173232.v1 (2020).
109. Quatredeniers, M. scRNA-seq dataset. Figshare https://doi.org/10.6084/m9.figshare.21587670.v1 (2022).
110. Quatredeniers, M. snRNA-seq dataset. Figshare https://doi.org/10.6084/m9.figshare.21587679.v1 (2022).

Acknowledgements

This research has been conducted using the UKB resource under application number 7089. We acknowledge the contributions of the UKB participants without whom this work would not have been possible. National Institutes of Health (NIH) T32HL007604 grant to V.N.; grants from the NIH (1RO1HL092577, 1R01HL157635 and 5R01HL139731), the American Heart Association (18SFRN34230127, 961045) and the European Union (MAESTRIA 965286) to P.T.E.; Scholar award from the Sarnoff Cardiovascular Research Foundation and NIH grant K08HL159346 to J.P.P.; NIH 1R01HL139731, NIH R01HL157635 and AHA 18SFRN34250007 grants to S.A.L.; NIH 5T32HL007208-42 grant to M.C.H.; Walter Benjamin Fellowship from the Deutsche Forschungsgemeinschaft (521832260) to S.K.

Author contributions

V.N. and P.T.E. conceived the study. M.D.R.K. ingested and prepared the MRI data. V.N., M.D.R.K., P.D.A. and J.T.R., performed QC. M.D.R.K. and D.F.P. trained machine learning models. V.N. and M.D.R.K. performed the main analyses. V.N., M.D.R.K. and P.T.E. wrote the paper. All other authors contributed to the analysis plan or provided critical revisions.

Competing interests

M.D.R.K., P.D.A and P.B. are supported by grants from Bayer AG and IBM applying machine learning in cardiovascular disease. P.B. has consulted for Novartis and Prometheus Biosciences. P.B. is now employed by Flagship Pioneering. P.D.A. is now employed by Google. S.A.L. is now employed by Novartis. S.A.L. received sponsored research support from Bristol Myers Squibb/Pfizer, Bayer AG, Boehringer Ingelheim, Fitbit and IBM, and has consulted for Bristol Myers Squibb/Pfizer, Bayer AG, Blackstone Life Sciences and Invitae previously. P.T.E. receives sponsored research support from Bayer AG, IBM Research, Bristol Myers Squibb, Pfizer and Novo Nordisk; and has also served on advisory boards or consulted for MyoKardia and Bayer AG. The remaining authors declare no competing interests.

Additional information

Supplementary information The online version contains supplementary material available at https://doi.org/10.1038/s41591-024-03010-w.

Correspondence and requests for materials should be addressed to Patrick T. Ellinor.

Peer review information *Nature Medicine* thanks David Brenner, Gerhard-Paul Diller, Yingkun Guo and Katalin Susztak for their contribution to the peer review of this work. Primary Handling Editor: Jerome Staal, in collaboration with the *Nature Medicine* team.

Reprints and permissions information is available at www.nature.com/reprints.

nature portfolio

Corresponding author(s): Patrick T. Ellinor

Last updated by author(s): 03/18/2024

Reporting Summary

Nature Portfolio wishes to improve the reproducibility of the work that we publish. This form provides structure for consistency and transparency in reporting. For further information on Nature Portfolio policies, see our Editorial Policies and the Editorial Policy Checklist.

Statistics

For all statistical analyses, confirm that the following items are present in the figure legend, table legend, main text, or Methods section.

n/a Confirmed

- [ ] [x] The exact sample size (*n*) for each experimental group/condition, given as a discrete number and unit of measurement
- [ ] [x] A statement on whether measurements were taken from distinct samples or whether the same sample was measured repeatedly
- [ ] [x] The statistical test(s) used AND whether they are one- or two-sided
  Only common tests should be described solely by name; describe more complex techniques in the Methods section.
- [ ] [x] A description of all covariates tested
- [ ] [x] A description of any assumptions or corrections, such as tests of normality and adjustment for multiple comparisons
- [ ] [x] A full description of the statistical parameters including central tendency (e.g. means) or other basic estimates (e.g. regression coefficient) AND variation (e.g. standard deviation) or associated estimates of uncertainty (e.g. confidence intervals)
- [ ] [x] For null hypothesis testing, the test statistic (e.g. *F*, *t*, *r*) with confidence intervals, effect sizes, degrees of freedom and *P* value noted
  Give P values as exact values whenever suitable.
- [x] [ ] For Bayesian analysis, information on the choice of priors and Markov chain Monte Carlo settings
- [x] [ ] For hierarchical and complex designs, identification of the appropriate level for tests and full reporting of outcomes
- [ ] [x] Estimates of effect sizes (e.g. Cohen's *d*, Pearson's *r*), indicating how they were calculated

Our web collection on statistics for biologists contains articles on many of the points above.

Software and code

Policy information about availability of computer code

Data collection	Code used to ingest, quality control, and train machine learning models are available at https://github.com/broadinstitute/ml4h under an open-source BSD license.
Data analysis	All statistical tests were performed using R version 4.0.2 (R Foundation for Statistical Computing, Vienna, Austria)(R, Core Team 2020). We defined diseases using v1.2 of the Phecode Map, which includes a set of 1,867 disease definitions arranged into clinically meaningful groups and identified using standardized sets of International Classification of Disease, 9th and 10th revision codes. PLINK 2.0 was used to perform genome wide association analysis. PLINK 1.9 was used to calculate in-sample linkage disequilibrium (LD) parameters. LD score regression analysis and genetic correlation were performed using ldsc version 1.0.0. Regional association plots were generated with LocusZoom.js v5.16.0. SNP-heritability was assessed using BOLT-REML v2.3.4. Cell-specific expression was analyzed using Seurat (version 4.3.0.1).

For manuscripts utilizing custom algorithms or software that are central to the research but not yet described in published literature, software must be made available to editors and reviewers. We strongly encourage code deposition in a community repository (e.g. GitHub). See the Nature Portfolio guidelines for submitting code & software for further information.

Data

Policy information about availability of data

All manuscripts must include a data availability statement. This statement should provide the following information, where applicable:

- Accession codes, unique identifiers, or web links for publicly available datasets
- A description of any restrictions on data availability
- For clinical datasets or third party data, please ensure that the statement adheres to our policy

UK Biobank data are made available to researchers from research institutions with genuine research inquiries, following IRB and UK Biobank approval. Genome-wide association analysis summary statistics are available from the Downloads page of the Cardiovascular Disease Knowledge Portal (broadcvdi.org). Genome Reference Consortium Human Build 37 (GRCh37) data is publicly available at https://www.ncbi.nlm.nih.gov/assembly/GCF_000001405.13/. Genome Reference Consortium Human Build 38 (GRCh38) data is publicly available at https://www.ncbi.nlm.nih.gov/assembly/GCF_000001405.26/. Single cell data for each organ were downloaded from: Liver, https://www.ncbi.nlm.nih.gov/geo/query/acc.cgi?acc=GSE185477 (GEO accession number GSE185477); Pancreas, https://doi.org/10.6084/m9.figshare.12173232; Heart, processed single cell data are available at https://singlecell.broadinstitute.org/single_cell/study/SCP1849/ and raw sequence data is available for authorized users at the database of Genotypes and Phenotypes, accession number phs001539.v4.p1; Kidney: https://figshare.com/articles/dataset/scRNA-seq_dataset/21587670 (single cell data) and https://figshare.com/articles/dataset/snRNA-seq_dataset/21587679 (single nucleus data).All other data are contained within the article and its supplementary information.

Research involving human participants, their data, or biological material

Policy information about studies with human participants or human data. See also policy information about sex, gender (identity/presentation), and sexual orientation and race, ethnicity and racism.

Reporting on sex and gender	We reported sex-specific distributions of organ-specific T1 time. In all other analyses, we adjust for sex as a covariate. In the UK Biobank, sex was self-reported by participants at enrollment.
Reporting on race, ethnicity, or other socially relevant groupings	The UK Biobank comprises individuals of predominantly European ancestry. We did not report ancestry-specific results as we were limited by the sample size of individuals with non-European ancestry. In our genome-wide association analysis we calculated principal components of genetic ancestry and adjusted for the first 10 principal components to account for population structure.
Population characteristics	The study sample included 43,881 participants with both multi-organ MRI T1 mapping performed during the first imaging visit and imputed genotype data in the UKB. The mean age of the participants was 64.2 ± 7.7 years and 48.1% were men. T1 mapping data for the liver, pancreas, heart, and renal cortex was available for 36,516, 33,862, 39,339 and 30,155 participants, respectively.
Recruitment	The UKB is a prospective cohort of 502,629 individuals from the UK enrolled between 2006-2010 with deep phenotyping, imaging and multiple genomic data types. Briefly, around 9.2 million individuals 40-69 years old living in England, Scotland, and Wales were invited to participate in the study and 5.4% agreed to participate. Extensive questionnaire data, physical measures, and biological samples were collected at baseline, with ongoing data collection in large subsets of the cohort, including repeated assessments and multimodal imaging. Starting in 2014, UKB participants were invited to return for the first multi-modal imaging visit including magnetic resonance imaging with T1 mapping of the liver, pancreas, kidneys, and heart allowing for the assessment of interstitial fibrosis in these organs. As of January 2022, 43,881 UKB participants had both imputed genetic data and T1 mapping data available. All study participants are followed longitudinally for health-related outcomes through linkage to national health-related datasets.
Ethics oversight	Use of UKB data was performed under application number 7089 and was approved by the local Massachusetts General Hospital institutional review board.

Note that full information on the approval of the study protocol must also be provided in the manuscript.

Field-specific reporting

Please select the one below that is the best fit for your research. If you are not sure, read the appropriate sections before making your selection.

☒ Life sciences ☐ Behavioural & social sciences ☐ Ecological, evolutionary & environmental sciences

For a reference copy of the document with all sections, see nature.com/documents/nr-reporting-summary-flat.pdf

Life sciences study design

All studies must disclose on these points even when the disclosure is negative.

Sample size	All UKB participants with T1 mapping data for the liver, pancreas, heart or renal cortex and imputed genomic data available were included. No power calculation was performed a priori. We identified multiple biologically plausible phenotypic and genomic associations with T1 time after accounting for multiple testing supporting that our examined sample study was well-powered to address our research aims.
Data exclusions	UKB participants who did not undergo MRI imaging or who did not have imputed genomic data were excluded from this study.
Replication	In deriving our measures of T1 time for each organ, we examined inter-reader reliability of our segmentation methods. We report inter-reader reliability metrics for measured T1 time for all organs. Unfortunately, we could not validate our study results in an independent cohort as there are currently no available population-based cohorts

	with paired genomic and multi-organ T1 mapping data. As the research and clinical applications of T1 mapping broaden and new multi-ancestry biorepositories emerge, further validation of our study findings will be possible.
Randomization	This is a prospective observational study and no randomization was performed.
Blinding	This is a prospective observational study and no blinding was performed.

Reporting for specific materials, systems and methods

We require information from authors about some types of materials, experimental systems and methods used in many studies. Here, indicate whether each material, system or method listed is relevant to your study. If you are not sure if a list item applies to your research, read the appropriate section before selecting a response.

Materials & experimental systems

n/a	Involved in the study
☒	☐ Antibodies
☒	☐ Eukaryotic cell lines
☒	☐ Palaeontology and archaeology
☒	☐ Animals and other organisms
☒	☐ Clinical data
☒	☐ Dual use research of concern
☒	☐ Plants

Methods

n/a	Involved in the study
☒	☐ ChIP-seq
☒	☐ Flow cytometry
☒	☐ MRI-based neuroimaging